

1 Modeling tabular icebergs coupled to an ocean model

2 **A. A. Stern¹, A. Adcroft¹, O. Sergienko¹, G. Marques¹, R. Hallberg¹**

3 ¹Geophysical Fluid Dynamics Laboratory, Princeton University

4 ¹201 Forrestal Rd, Princeton, NJ 08540, USA

5 **Key Points:**

- 6 • A novel modeling framework is developed to explicitly model large tabular icebergs
7 submerged in the ocean.
- 8 • Tabular icebergs are represented using Lagrangian elements that drift in the ocean,
9 and are held together by numerical bonds.
- 10 • Breaking the numerical bonds allows us to model iceberg breakup and calving.

11 **Abstract**

12 Large tabular icebergs calved from Antarctic ice shelves have long lifetimes (due to their
 13 large size), during which they drift across large distances, altering ambient ocean circulation,
 14 bottom-water formation, sea-ice formation and biological primary productivity in the
 15 icebergs' vicinity. However, despite their importance, the current generation of ocean cir-
 16 culation models do not represent large tabular icebergs. In this study we develop a novel
 17 framework to model large tabular icebergs submerged in the ocean. In this framework,
 18 tabular icebergs are represented by Lagrangian elements that drift in the ocean, and are
 19 held together and interact with each other via bonds. A break of these bonds allows the
 20 model to emulate calving events (i.e. detachment of a tabular iceberg from an ice shelf)
 21 and tabular icebergs breaking up into smaller pieces. Idealized simulations of a calving
 22 tabular iceberg, its drift, and breaking into two pieces, demonstrate capabilities of the de-
 23 veloped framework.

24 **1 Introduction**

25 Large tabular icebergs - pieces of floating ice with horizontal dimensions substan-
 26 tially larger than the vertical dimension - calve infrequently (~ every forty-fifty years)
 27 from Antarctic or Greenlandic ice shelves [Jacobs et al, 1992]. Observational estimates
 28 suggest that over the past 30 years approximately half of Antarctic ice-shelf decay is due
 29 to iceberg calving, while the other half occurs through ice-shelf melting [Depoorter et
 30 al, 2013; Rignot et al, 2013]. The infrequently-calved tabular icebergs (horizontal extent
 31 larger than 5 km) account for more than 90% of the Southern Hemisphere iceberg mass
 32 [Tournadre et al, 2016].

33 After calving, icebergs drift away from their origins, often becoming stuck in sea
 34 ice, or grounding on bathymetric highs along the Antarctic coast [Lichy and Hellmer,
 35 2001; Dowdeswell and Bamber, 2007]. Large tabular icebergs extend deep into the water
 36 column, and have the potential to disrupt ocean circulation patterns for months or even
 37 years after calving [Robinson et al, 2012; Stern et al, 2015]. The freshwater flux from
 38 iceberg melt impacts ocean hydrography around the iceberg, influencing sea-ice produc-
 39 tion and bottom-water formation [Arrigo et al, 2002; Robinson et al, 2012; Nicholls et al,
 40 2009; Fogwill et al, 2016]. Because of their large size, the tabular icebergs have long life-
 41 times during which they drift over long distances injecting meltwater along the way and
 42 impacting the Southern Ocean state (e.g. hydrography, sea ice conditions, etc.) far away
 43 from their calving origins [Stern et al, 2016; Rackow et al, 2017]. Meltwater injection
 44 (and the accompanying upwelling) from icebergs can also influence biological productiv-
 45 ity by bringing nutrients to the surface ocean or changing sea ice conditions [Arrigo et al,
 46 2002; Vernet et al, 2012; Biddle et al, 2015]. The increased productivity associated with
 47 free-floating tabular icebergs has been linked with local increases in ocean carbon uptake,
 48 potentially large enough to be a significant fraction of the Southern Ocean carbon seques-
 49 tration [Smith et al, 2007].

50 In recent years, there has been an increased interest in iceberg drift and decay. This
 51 surge of interest has been driven by (i) the need to understand polar freshwater cycles in
 52 order to create realistic climate change and sea level projections [Silva et al, 2006; Shep-
 53 herd and Wingham, 2007; Rignot et al, 2013]; and (ii) the increased navigation and explo-
 54 ration activities in high-latitude iceberg-filled waters in the Arctic [Pizzolato et al, 2012;
 55 Unger, 2014; Henderson and Loe, 2016]. The increased interest in icebergs has led to the
 56 development of numerical models of iceberg drift and decay [Mountain, 1980; Bigg et
 57 al, 1997; Gladstone et al, 2001; Kubat et al, 2005], some of which have been included in
 58 global General Circulation Models [Martin and Adcroft, 2010; Marsh et al, 2015]. These
 59 iceberg drift models treat icebergs as Lagrangian point particles, which are advected by
 60 the flow, and melt according to parameterizations for icebergs melt. Since icebergs are
 61 treated as point particles, iceberg drift models are mostly suitable for modeling icebergs

62 smaller than an ocean grid cell. Consequently, these models have mostly been used to rep-
 63 resent icebergs smaller than 3.5 km on a global scale [Jongma et al, 2009; Martin and
 64 Adcroft, 2010; Marsh et al, 2015].

65 Point-particle iceberg drift models are less suitable for modeling larger tabular ice-
 66 bergs, where the size and structure of the iceberg may be an important feature in deter-
 67 mining their drift and decay [Stern et al, 2016]. They also are not suitable for studying
 68 the local effects that icebergs have on the surrounding ocean, or the small scale processes
 69 that influence iceberg melt and decay [Wagner et al, 2014; Stern et al, 2015]. For these
 70 reasons, tabular icebergs are currently not represented in the iceberg drift models used as
 71 components of climate models, despite accounting for the vast majority of the total South-
 72 ern Hemisphere iceberg mass [Tournadre et al, 2016]. Point-particle iceberg models also
 73 do not have any representation of iceberg breakup and calving, which is known to be an
 74 important iceberg decay mechanism that influences iceberg trajectories.

75 The goal of this study is to develop a new framework to model all kinds of icebergs,
 76 where tabular icebergs are explicitly resolved in the ocean. Our new representation of ice-
 77 bergs aims to include the following key properties: (i) icebergs should be able to travel
 78 large distances within the ocean, (ii) icebergs should melt and decay as they drift in the
 79 ocean, (iii) icebergs should behave as if they have finite extent (in order to study local
 80 effects that icebergs have on the surrounding ocean), and (iv) tabular icebergs should be
 81 able to break away from ice shelves or break into smaller pieces. Properties (i) and (ii)
 82 are common to point-particle iceberg models, while properties (iii) and (iv) are new to
 83 the framework developed in this study. A further requirement of the new framework is
 84 that the model should run sufficiently quickly to be used in general circulation models
 85 used for climate.

86 In order to allow icebergs to travel large distances, we model the icebergs in a La-
 87 grangian framework (as in the point particle iceberg drift models described above). How-
 88 ever in our model icebergs are no longer treated as point particles that interact with the
 89 ocean at a single location. Instead icebergs are given physical structure, so that they inter-
 90 act with the ocean across multiple ocean grid cells, depress the ocean surface over a wide
 91 area, and can interact with other icebergs (Figure 1). This is done by assigning a finite
 92 surface area and shape to the Lagrangian elements, which allows the elements to behave
 93 as if they have a finite extent. The finite extent of an element is transmitted by the ocean
 94 by distributing the element's weight, surface area and melt fluxes over multiple ocean grid
 95 cells in a way which is consistent with the shape of the ice element. Finite-extent ele-
 96 ments interact with each other via repulsive forces which are applied when the boundaries
 97 of the elements overlap.

98 Large tabular icebergs can then be represented by ‘bonding’ together multiple ice el-
 99 ements into larger structures using numerical bonds (Figure 1). The numerical bonds hold
 100 the ice elements together and allow a collection of elements to move as a unit. This al-
 101 lows tabular icebergs to drift in the ocean when forced by ocean currents and wind. An
 102 advantage of representing tabular icebergs using numerical bonds is that by breaking the
 103 bonds, we can simulate iceberg calving (e.g.: Figure 2), or the response to an iceberg frac-
 104 turing into multiple smaller pieces.

105 The manuscript is organized as follows. Section 2 gives a description of the key
 106 aspects of the model developed in this study. Since this model is a new approach to mod-
 107 eling icebergs, we present technical aspects of the model. In Sections 3 and 4, we demon-
 108 strate the capabilities of the model by simulating a tabular iceberg detaching from an ide-
 109 alized ice shelf. In a further simulation we break some numerical bonds within the tabular
 110 iceberg to demonstrate an iceberg splitting in two.

111 2 Model description

112 The Lagrangian Bonded Iceberg Model (LBIM) is a Lagrangian particle-based model
 113 in that the objects of the model are Lagrangian elements. Each element represents a col-
 114 umn of ice that is floating in the ocean, and has a position, velocity, mass, and a set of
 115 dimensions, which can evolve in time. The motion of each element is determined by a
 116 momentum equation which is solved in the (Lagrangian) reference frame of the element.
 117 The elements experience oceanic and atmospheric forces, which are either prescribed, or
 118 computed by coupling the LBIM to an ocean/atmosphere model. The LBIM elements also
 119 interact with one another via attractive and repulsive interactive forces, and can be bonded
 120 together to form larger structures. The angular momentum of the elements is not modeled
 121 explicitly; instead rotational motion of larger structures emerge as a consequence of bond
 122 orientation and collective motion.

123 In different contexts, the LBIM elements can be thought to represent individual ice-
 124 bergs, sea ice flows, or, when the elements are bonded together, they can represent larger
 125 structures such as tabular icebergs or ice shelves.

126 The LBIM is developed on the code base of an existing iceberg drift model [Martin
 127 and Adcroft, 2010; Stern et al, 2016]. When run with the correct set of runtime flags, the
 128 model runs as a traditional point-particle iceberg drift model.

129 2.1 Equations of motion

130 The elements drift in the ocean in response to atmosphere, ocean and sea-ice drag
 131 forces, as well as the Coriolis force, a wave radiation force, a force due to the sea sur-
 132 face slope and interactive forces with other elements. The momentum equation for each
 133 element is given by

$$134 M \frac{D\vec{u}}{Dt} = \vec{F}_A + \vec{F}_W + \vec{F}_R + \vec{F}_C + \vec{F}_{SS} + \vec{F}_{SI} + \vec{F}_{IA}, \quad (1)$$

135 where $\frac{D}{Dt}$ is the total (Lagrangian) derivative, M is the mass of the element, \vec{u} is the ve-
 136 locity of the element, and the terms on the right hand side give the forces on the element
 137 due to air drag (\vec{F}_A), water drag (\vec{F}_W), sea ice drag (\vec{F}_{SI}), Coriolis force (\vec{F}_C), wave radi-
 138 ation force (\vec{F}_R), sea surface slope (\vec{F}_{SS}), and interactions with other elements (\vec{F}_{IA}).

139 When ice elements move alone (without interactions with other elements), they can
 140 be thought of as representing individual (or clusters of) small icebergs, and follow the
 141 same equations described in the iceberg drift model of Martin and Adcroft [2010] (based
 142 on the equations outlined in Bigg et al [1997] and Gladstone et al [2001]). These environ-
 143 mental forces are provided for completeness in Appendix A.

144 In addition to the external forces, the elements in the LBIM experience interactive
 145 forces due to the presence of other elements. Two types of interactive forces are included
 146 between elements. The first force is a repulsive force which is applied to elements to pre-
 147 vent them from overlapping the boundaries of the neighboring elements. The second in-
 148 teractive force is a force due to numerical ‘bonds’, and is only applied if two elements
 149 are labelled as ‘bonded’. When two elements are bonded, each element feels an attractive
 150 force that prevents the elements from moving too far apart from one another. The details
 of the interactive forces are provided in below.

151 2.2 Interactive Forces

152 The interactive forces in the model are used to (i) prevent the ice elements from
 153 overlapping and (ii) to connect multiple ice elements together so that the collection of el-
 154 ements moves as a rigid body. Modeling the collisions and movements of rigid objects
 155 precisely, requires very small time steps and precise collision detection algorithms, which

are very computationally expensive. Models using these methods are typically only run for a few days or even a few seconds, and are used to study rapid processes like crack formation or ridging [Hopkins, 2004; Bassis and Jacobs, 2013; Rabatel et al, 2015]). The tabular iceberg framework presented in this study is developed in order to be used in general circulation models used for multi-year simulations. In order to gain the required computational efficiency, we relax the requirement that icebergs must be perfectly rigid and that ice elements can not overlap. Instead, we model the interactive forces between ice elements using damped elastic forces, which can be calculated more efficiently.

The total interactive force on an element is calculated by adding together the interactions with all other elements, such that the interactive force on element i , $(\vec{F}_{IA})_i$ is given by:

$$(\vec{F}_{IA})_i = \sum_{j \neq i} (\vec{F}_{IA})_{ij}, \quad (2)$$

where $(\vec{F}_{IA})_{ij}$ is the force on element i by element j . Both bonded and repulsive interactions are modeled using elastic stresses with frictional damping. The elastic component of the force is a function of the distance between the two elements, while the frictional damping force depends on the relative velocity of the two elements.

To describe the forces between two elements, we begin by introducing some notation. Let \vec{x}_i , \vec{x}_j be the positions of elements i and j . The distance between elements i and j is

$$d_{ij} = |\vec{x}_i - \vec{x}_j|. \quad (3)$$

In calculations of the interactive forces between elements, the elements are assumed to be circular. We define the interaction radius of an element by

$$R_i = \sqrt{\frac{A_i}{\pi}}, \quad (4)$$

where A_i is the planar surface area of element i . Using this, we define the critical-interactive-length scale,

$$L_{ij} = R_i + R_j, \quad (5)$$

which governs interactions between elements i and j . Repulsive forces are only applied when $d_{ij} < L_{ij}$, while for $d_{ij} > L_{ij}$ attractive bonded forces are applied when a bond exists between element i and j (see diagram in Figure 3). The interactive forces are designed such that (in the absence of other external forces) bonded particles will settle in an equilibrium position where elements are separated by L_{ij} .

To aid in notation, we define a bond matrix B_{ij} such that $B_{ij} = 1$ if elements i and j are bonded together and $B_{ij} = 0$ otherwise. Using this notation, the interactive force $(\vec{F}_{IA})_{ij}$ on an element i by an element j is given by

$$(\vec{F}_{IA})_{ij} = \begin{cases} (\vec{F}_e)_{ij} + (\vec{F}_d)_{ij} & \text{if } d_{ij} \leq L_{ij} \\ (\vec{F}_e)_{ij} + (\vec{F}_d)_{ij} & \text{if } d_{ij} > L_{ij} \text{ and } B_{ij} = 1 \\ 0 & \text{if } d_{ij} > L_{ij} \text{ and } B_{ij} = 0 \end{cases} \quad (6)$$

$(\vec{F}_e)_{ij}$ and $(\vec{F}_d)_{ij}$ are the elastic and frictional damping components of the interactive force between elements i and j . The elastic force $(\vec{F}_e)_{ij}$ between elements is given by

$$(\vec{F}_e)_{ij} = -\kappa_e (d_{ij} - L_{ij}) M_{i,j} \vec{r}_{ij}, \quad (7)$$

where $\vec{r}_{ij} = \frac{(\vec{x}_i - \vec{x}_j)}{|\vec{x}_i - \vec{x}_j|}$ is the directional unit vector between the position of element i and j , κ_e is the spring constant, and $M_{i,j}$ is the minimum of the masses of elements i and j . The interactive forces obey Newton's 3rd Law (i.e.: $(\vec{F}_{IA})_{ij} = -(\vec{F}_{IA})_{ji}$). The minimum mass, $M_{i,j}$, is preferred to the average thickness, since this means that for two bonded elements a fixed distance apart, the acceleration due to elastic forces is bounded, even when the thickness of one of the elements approaches zero.

194 The frictional damping force acts to dampen the relative motion of the two particles.
 195 If \vec{r}_{ij}^\perp is the direction vector perpendicular to \vec{r}_{ij} , and $P_{\vec{r}_{ij}}$ and $P_{\vec{r}_{ij}^\perp}$ are the projection ma-
 196 trices that project onto \vec{r}_{ij} and \vec{r}_{ij}^\perp respectively, then the frictional damping force is given
 197 by

$$(F_d)_{ij} = \left(-c_{r\parallel} P_{\vec{r}_{ij}} - c_{r\perp} P_{\vec{r}_{ij}^\perp} \right) \cdot (\vec{u}_i - \vec{u}_j) \quad (8)$$

198 Here $c_{r\parallel}$ and $c_{r\perp}$ are the drag coefficients for the damping motion parallel and perpen-
 199 dicular to r_{ij} , respectively. We set $c_{r\parallel} = 2\sqrt{\kappa_e}$, so that the elastic force parallel to \vec{r}_{ij} is
 200 critically damped. The perpendicular drag coefficient is set to $c_{r\perp} = \frac{1}{4}c_{r\parallel}$. The perpen-
 201 dicular damping force is used reduce the relative motion of ice elements passing by one
 202 another with overlapping boundaries. The damping forces are implemented using an im-
 203 plicit time stepping scheme, to avoid stability issues for very small elements (details found
 204 in Appendix B).

205 Figure 4 illustrates the effectiveness of the repulsive forces in an uncoupled (ice-
 206 only) simulation of ice elements forced to drift westward into a bay. The elements even-
 207 tually come to rest in the bay with minimal overlap between elements. Figure 5 illustrates
 208 the effectiveness of the numerical bonds in simulations of small icebergs (individual un-
 209 bonded elements) and large icebergs (constructed from many ice elements bonded to-
 210 gether) forced to drift towards a convex coast line. When the tabular icebergs arrive at the
 211 coast, they bump into the coastline and begin to rotate, influencing the paths of the other
 212 icebergs (movies S1 and S2 in the Supporting Information). This example illustrates an
 213 advantage of using small elements bonded together, to represent large-scale structure and
 214 rotational motion without explicitly accounting for the angular momentum of the elements
 215 (as discussed in Jakobsen [2001]).

2.3 Initializing element geometry and packing

217 For purposes of initialization, we assume that elements have surface areas which are
 218 shaped as equally-sized regular hexagons (note that the elements are assumed to be circu-
 219 lar for proposes of interactions). When packing elements together, the hexagonal elements
 220 are initially arranged in a staggered lattice, with each element bonded to the adjacent el-
 221 ements (Figure 6a). In this arrangement, each element (away from the edges) is bonded
 222 to six other elements. The bonds between elements form a pattern of equilateral triangles,
 223 which gives rigidity to the larger structure. The circular shape of elements (used for inter-
 224 actions) is inscribed within the hexagonal shape used for packing (Figure 6a). The centers
 225 of adjacent elements are initially separated by a distance $d_{i,j} = L_{i,j} = 2A_p$, where A_p is
 226 the length the apothems of the hexagons.

227 Some experiments were also performed using rectangular elements, arranged in a
 228 regular (non-staggered) lattice. In this case, each element forms four bonds with adjacent
 229 elements. However, the resultant structures were found to be much less rigid and tended
 230 to collapse when sufficient forces was applied. For this reason, we only show the results
 231 using hexagonal elements.

2.4 Ocean-ice and ice-ocean coupling

233 The LBIM is coupled to the ocean model via a two-way synchronous coupling,
 234 meaning that ocean-model fields are passed to the LBIM, and the LBIM fields are passed
 235 back to the ocean model at every time step. Passing fields between the two models in-
 236 volves interpolating the fields from the ocean model's Eulerian grid onto the LBIM's 'La-
 237 grangian grid' (i.e.: onto the ice elements), and aggregating fields from the Lagrangian
 238 elements onto the ocean-model's Eulerian grid.

239 The coupling from the ocean model to the LBIM is straight forward: at every time
 240 step: the ocean mixed layer temperature, salinity, velocity and sea-ice concentration are

241 passed from the ocean model to the LBIM, to be used in the momentum and thermo-
 242 dynamic equations of the ice elements. Since tabular icebergs are explicitly resolved in
 243 the ocean, it is sufficient for each element to interact with ocean mixed layer only (i.e.:
 244 there is no need to manually embed icebergs into the ocean by integrating ocean fields
 245 over the icebergs' thickness, as suggested in Merino et al [2016]). Within the LBIM, the
 246 ocean model fields are interpolated onto the Lagrangian grid using a bilinear interpolation
 247 scheme.

248 The LBIM influences the ocean by: (i) applying a pressure to the ocean surface, (ii)
 249 affecting the upper ocean by applying a no-slip boundary condition and frictional velocity
 250 beneath the ice, and (iii) imposing heat, salt and mass fluxes on the ocean, associated with
 251 ice melting. Six fields are passed from the LBIM to the ocean model: ice mass, ice area,
 252 frictional velocity, and heat, salt and mass fluxes. Fields from the LBIM are aggregated
 253 from the Lagrangian elements to the Eulerian ocean grid before they are passed to the
 254 ocean model.

255 The aggregation of the LBIM fields onto the ocean grid is done in a way that is
 256 consistent with the shape of the elements in the LBIM (see Section 2.3). Fields are 'spread'
 257 to the ocean model grid by exactly calculating what fraction of an element's surface area
 258 lies in a particular grid box, and dividing the field in proportion to this fraction. As an
 259 example, consider a hexagonal element in the LBIM, which is positioned such that it in-
 260 tersects four ocean grid cells (Figure 6b). In this situation, the element's mass (for exam-
 261 ple) is divided between these four ocean cells in proportion to the overlap area between
 262 the hexagonal element and the grid cell (this fraction is shown by the colors in Figure
 263 6b). An advantage of this approach is that there are no jumps in pressure as an element
 264 moves from one grid cell to another, which could trigger artificial tsunamis within the
 265 ocean model, making the ocean model unrealistic.

266 The numerical calculation of the intersection between hexagons and the ocean grid
 267 is simplified by dividing the hexagon into 6 equilateral triangles. This method allows for
 268 the intersection to be found even when the hexagon is not aligned with the grid.

269 The aggregation scheme is coded with the restriction that an element's area can only
 270 intersect a maximum of four ocean grid cells at a time. A consequence of this is that this
 271 sets a limit on the maximum size of elements that can be represented using this model,
 272 i.e.: the longest horizontal dimension of an ice element must be smaller than the ocean
 273 grid spacing. Larger ice structures are constructed by bonding together smaller elements.

274 2.5 Melting parameterization

275 The ice elements change their mass and size due to melting, which also affects the
 276 surrounding ocean by changing its heat and salt content. In the model, these processes are
 277 parametrized in several ways. In this section we described the melt parametrization for
 278 bonded, unbonded and partially bonded elements.

279 As mentioned above, ice elements which do not interact with other elements are
 280 modeled identically to the point particle icebergs described in Martin and Adcroft [2010].
 281 These elements melt according to three semi-empirical parametrization for melt commonly
 282 used in previous iceberg studies [Gladstone et al, 2001; Martin and Adcroft, 2010]. Three
 283 types of iceberg melting are distinguished: basal melt, M_b , melt due to wave erosion, M_e
 284 and melt due to buoyant convection, M_v . M_e and M_v are applied to the sides of the ice
 285 element, while M_b is applied at the ice element base. The details of M_b , M_v and M_e are
 286 given in Appendix A.

287 When multiple elements are bonded together to form larger structures, it is no longer
 288 appropriate to use the parameterizations for melt developed for individual point-particle
 289 icebergs. An element which is completely surrounded by other elements, is meant to rep-

resent a column of ice in the middle of a large structure, and hence will not experience melt at its sides due to wave erosion or buoyant convection. Also, the iceberg basal melt rate, M_b described above is based on boundary layer theory of flow past a finite plate, and is only appropriate for basal surfaces where the distance from the leading edge is sufficiently small [Eckert, 1950; Weeks and Campbell, 1973]. For an element in the interior of a large structure, the distance from the edge of the structure is large, and so using M_b for the basal melt is not appropriate. Instead, the basal melt, M_s is determined using the three equation model for basal melt, which is a typical melting parametrization used beneath ice shelves [Holland and Jenkins, 1999].

When using both individual elements and bonded elements in the same simulation, we determine which melt rate parameterizations to use based on the amount of bonds that each element has. An element in the center of a large structure has the maximum number of bonds, while un-bonded elements has no bonds. If an element can have maximum number of bonds N_{max} , and the number bonds that an element has is N_b , then this element experiences the side melt and bottom melt

$$M_{side} = \frac{(N_{max} - N_b)}{N_{max}}(M_v + M_e) \quad (9)$$

and

$$M_{bottom} = \frac{(N_{max} - N_b)}{N_{max}}M_b + \frac{N_b}{N_{max}}M_s \quad (10)$$

respectively. In this way, elements with no bonds, melt like point-particle icebergs; elements at the center of large structures melt like ice shelves; and elements at the sides of large structures have a combination of iceberg side and basal melt, and ice-shelf melt.

2.6 Algorithms and computational efficiency

Including interactions between elements leads to an increase in the computational complexity of the model. In this subsection we comment on some of the algorithmic procedures that have been used to increase the computational efficiency.

2.6.1 Interactions and Bonds

At every time step, we calculate the force on each element due to interactions with every other element. This involves order N^2 operations (for N elements), which becomes computational expensive as N grows large. We reduce the number of computations by leveraging the fact that each element only has repulsive interactions with elements that are less than one ocean grid cell away, and each element only has bonded interactions with a small number of other elements.

The computation reduction is achieved by storing the element data in an efficient way that eliminates a search through all element pairs to check if they are close to one another or are bonded with one another. The data storage system is organized as follows: pointers to the memory structures containing each element are stored in linked list data structures, which allow elements to be added and removed from the lists easily without restructuring the entire list. Instead of using one list for all the elements on a processor (as was done in the original code [Martin and Adcroft, 2010]), we use a separate linked list for each ocean grid cell. When an element moves between ocean grid cells, it is removed from its original list and added to the list corresponding to its new ocean grid cell. Since the area of elements has to be smaller than the area of an ocean grid cell, the critical interaction length scale (equation 5) is less than the size of a grid cell. This means that elements only experience repulsive forces with other elements in the same ocean grid cell, or in one of the 8 adjacent cells. At each time step and for each element i , the code traverses the linked lists of the 9 surrounding grid cells, and applies a repulsive force if $d_{i,j} < L_{ij}$ (whether the elements are bonded or not). Limiting the possible repulsive in-

335 teractions to elements in these 9 linked lists substantially reduces the computational time
 336 needed to calculate the total interactive forces.

337 The attractive forces are computed in a following way. Each bond is assigned a
 338 piece of memory. Each ice element contains a linked list of each of its bonds (typically
 339 up to six bonds per element). At every time step, the code traverses the lists of bonded
 340 elements, and adds an attractive bonded force corresponding to these bonds if $d_{i,j} > L_{ij}$
 341 (the repulsive bonded force to be applied when $d_{i,j} < L_{ij}$ is already accounted for by
 342 the procedure outlined in the previous paragraph). Having a list of bonds stored with each
 343 element reduces the computations needed for bonded interactions from order N^2 to or-
 344 der N. Computing attractive forces separately from the repulsive forces allows us to avoid
 345 checking whether two elements are bonded, which further increases the computational effi-
 346 ciency.

347 **2.6.2 Parallelization and halos**

348 The LBIM runs on multiple processors in parallel (using the same grid decomposi-
 349 tion as the ocean model). When elements move from an ocean cell on one processor to
 350 an ocean cell on a second processor, the memory has to be passed from one processor to
 351 the next, added and removed to the appropriate lists and the memory has to be allocated and
 352 deallocated correctly. Element interactions across the edge of processors are handled using
 353 computational halos. A computational halo is a copy of the edge of a one processor which
 354 is appended to the edge of a second processor, so that the first processor can interact with
 355 the second processor during a time step. Before each time step, elements at the edges of
 356 each processor are copied onto the halos of adjacent processors so that they can be used
 357 in calculating the interactive forces. After each time step, these halos are emptied, and the
 358 process is repeated. These halo updates are one of the most computationally expensive
 359 parts of the LBIM. Details of how the bonds are broken and reconnected across processor
 360 boundaries are provided in Appendix C.

361 **2.6.3 Time stepping**

362 The elements in the LBIM are advected using a semi-implicit velocity Verlet time-
 363 stepping scheme. The velocity Verlet time stepping scheme is commonly used in discrete
 364 element models in video games because it is computational efficient and has desirable sta-
 365 bility properties [Jakobsen, 2001]. This time stepping scheme was preferred to the Runge-
 366 Kutta 4, which was used in the iceberg model of Martin and Adcroft [2010] since the
 367 Verlet time stepping only requires one calculation of the interactive forces once per time
 368 step (while the Runge-Kutta scheme requires the interactive forces to be calculated four
 369 times). Since the calculation of the interactive forces is one of the most computationally
 370 expensive part of the algorithm, the Verlet scheme leads to a significant increase in the
 371 computational efficiency of the model. The Verlet scheme used in the LBIM contains a
 372 modification of the original (fully explicit) velocity Verlet time stepping scheme in that
 373 damping terms are treated implicitly (which increases the numerical stability). The details
 374 of this time stepping scheme are outlined in Appendix B.

375 **3 Experiment Setup**

376 The introduction of Lagrangian elements, numerical bonds and interpolation schemes
 377 between the Eulerian and Lagrangian grids (discussed in Section 2) means that we now
 378 have the tools to model large tabular icebergs submerged in the ocean. We demonstrate
 379 this capability by simulating a tabular iceberg drifting away from an ice shelf in idealized
 380 setting.

381 3.1 Model configuration

382 We use the geometric setup of the Marine Ice Ocean Modeling Inter-comparison
 383 Project (MISOMIP) [Asay-Davis et al, 2016]. The configuration consists of an idealized
 384 ice shelf in a rectangular domain. The domain is $L_x = 80$ km wide and $L_y = 480$ km
 385 long, and contains an ice shelf which is grounded on the south side of the domain and
 386 has an ice front at $y=650$ km. The ice thickness and bottom topography of this setup are
 387 shown in Figure 7a and 7c respectively, with the grounding line position drawn in for ref-
 388 erence. The configuration is the same as that of the Ocean0 setup in the MISOMIP, with a
 389 few minor changes to the ice-shelf geometry (see Supporting Information for details).

390 3.2 Initializing Lagrangian elements:

391 The idealized ice shelf is constructed out of Lagrangian ice elements. Ice elements
 392 are hexagonal and are arranged in a regular staggered lattice (as discussed in Section 2.3).
 393 The sides of the hexagons are initialized with length $S = 0.98$ km. Gaps along the bound-
 394 aries are filled in using smaller elements so that the total ice-shelf area is preserved. The
 395 initial mass of the ice elements is determined by a preprocessing inversion performed be-
 396 fore the model is run. When the model runs, the mass of elements is aggregated from the
 397 Lagrangian grid onto the Eulerian ocean grid (see Section 2.3), and is used to find the
 398 surface pressure and ice draft (part of an ice column submerged into the ocean). The ice
 399 draft calculated without the aggregation (treating elements as point masses) contains large
 400 grid artifacts (Figures 7b). These grid artifacts are much reduced after the mass-spreading
 401 aggregation is used (Figure 7c).

402 3.3 Ocean model setup

403 The LBIM is coupled to the MOM6 ocean model [Hallberg et al, 2013]. The ocean
 404 model configuration uses a vertical coordinate system which is a hybrid between a sigma-
 405 level and a z-level coordinate. In particular, model layers deform underneath the ice shelf
 406 as they would in a sigma-coordinate model, but collapse to zero thickness when they in-
 407 tersect with bottom topography, as they would in a z-level model. The coordinate system
 408 was achieved using ALE regridding-remapping scheme [White et al, 2009]. The model
 409 uses a horizontal resolution of 2 km, and 72 vertical layers. All simulations were repeated
 410 using the ocean model configured in isopycnal mode (results were similar and are not pre-
 411 sented here).

412 Ocean parameters are as specified in the MISOMIP configuration [Asay-Davis et
 413 al, 2016], and are shown in Table 1. The simulation is initially at rest, with horizontally
 414 uniform initial ocean temperature and salinity profiles which vary linearly between spec-
 415 ified surface and bottom values: $T_{top} = -1.9^\circ$ C, $T_{bottom} = 1.0^\circ$ C, $S_{top} = 33.8$ psu,
 416 $S_{bottom} = 34.7$ psu. The maximum ocean depth is $H_{ocean} = 720$ m. A sponge layer is
 417 used on the northern boundary of the domain, which relaxes the temperature and salinity
 418 back to the initial temperature and salinity profile. The sponge layer has length L_{sponge}
 419 = 10 km, and has a relaxation time scale parameter $T_{sponge} = 0.1$ days at the northern
 420 boundary. The inverse of the relaxation time scale parameter drops linearly to zero over
 421 the length of the sponge layer. Melting is set to zero for ocean cells where the ocean col-
 422 umn thickness is less than 10m to avoid using more energy to melt ice than is present in
 423 the water column.

424 3.4 Spinup period:

425 The model is spun-up for 5 years with all ice elements being fixed. During spinup,
 426 the injection of buoyant meltwater at the base of the ice shelf drives a clockwise circu-
 427 lation within the domain (not shown). The circulation compares well with an identical
 428 static ice-shelf experiment run using an Eulerian ice shelf model [Goldberg et al, 2012].

429 A detailed comparison of the Lagrangian and Eulerian ice shelf models is presented in a
 430 separate study, and is not shown here.

431 **3.5 Iceberg calving:**

432 After spinup, a large tabular iceberg detaches from the ice shelf, and is allowed to
 433 drift into the open ocean. This is achieved by allowing all ice elements initially within a
 434 14.4 km radius of the center of the ice front to move freely while the other ice elements
 435 continue to be held stationary. Ice elements less than 12 km from the center of the ice
 436 front, are bonded together to form a semi-circular tabular iceberg. A ring of elements
 437 whose distance, d , from the ice front center obeys $12 \text{ km} \leq d \leq 14.4 \text{ km}$, are allowed
 438 to move freely, but have all their bonds removed. Elements in this half annulus represent
 439 fragments of the ice shelf which calve into small pieces during the calving event.

440 After the spinup period, a wind stress $\vec{\tau} = <\tau_x, \tau_y> = <0.05, 0.05> \frac{\text{N}}{\text{m}^2}$ is applied to
 441 drive the tabular iceberg away from the ice-shelf cavity. This is referred to as the Control
 442 simulation. Perturbation experiments were also performed using other wind stress values.
 443 Further perturbation experiments were performed by breaking some numerical bonds in
 444 order to break the tabular iceberg into smaller pieces.

445 **4 Model Results**

446 After spinup of the Control simulation, the elements near the ice-shelf front are al-
 447 lowed to move freely, and the icebergs begin to drift away from the ice shelf while fully
 448 submerged in the ocean (see Figures 2 and 8, and the movies in the Supporting Infor-
 449 mation). At this point, the LBIM and the ocean model are fully coupled: changes to
 450 the iceberg position alter the top-of-ocean pressure and dynamical boundary condition;
 451 and changes to the iceberg melt rates alter the top-of-ocean temperature, salt and mass
 452 fluxes. These changing ocean boundary conditions influence the ocean by triggering grav-
 453 ity waves, driving surface mixing, and affecting the ocean stratification. The evolving
 454 ocean velocities, temperatures and salinities feedback onto the ice elements by changing
 455 the force balance on the ice elements (leading to changes in the elements' position), and
 456 altering the melt rates. The various feedbacks within this coupled system offer many op-
 457 portunities for the model to become unstable. The fact that the model is stable and that
 458 we are able to simulate tabular icebergs moving in the ocean without the modeling crash-
 459 ing and introducing artificial effects like tsunamis, is a non-trivial technical milestone.

460 **4.1 Iceberg motion**

461 In the Control simulation, the semi-circular tabular iceberg moves as a cohesive unit
 462 due to the presence of the numerical bonds, while the smaller ice fragments quickly dis-
 463 perse (Figure 2). The tabular iceberg drifts towards the north east, driven by the wind and
 464 steered by the Coriolis force. As the tabular iceberg drifts northwards, it rotates in a coun-
 465 terclockwise direction (the direction of the Coriolis force in the Southern Hemisphere),
 466 and makes contact with the eastern boundary of the domain, before continuing northward.
 467 Most of the smaller ice fragments also move to the northeast, but not as a cohesive unit.
 468 Some of these element also move to other parts of the domain.

469 The direction (and speed) of the iceberg drift is largely determined by the wind
 470 speed and direction. Perturbation experiments using different wind stresses show that for
 471 sufficiently large winds, the tabular iceberg drifts to the north east when $\tau_x > 0$, and to the
 472 north west when $\tau_x < 0$ (not shown). For a purely zonal wind stress with $|\tau_x| \leq 0.01 \frac{\text{N}}{\text{m}^2}$,
 473 the iceberg does not move away from the ice shelf. When the wind is purely offshore
 474 ($\tau_x = 0.0 \frac{\text{N}}{\text{m}^2}$), a meridional wind stress $\tau_y \geq 0.05 \frac{\text{N}}{\text{m}^2}$ is needed to move the tabular ice-
 475 berg away from the ice shelf. While this result is partly an artifact of the chosen shape
 476 of the calving iceberg, it is also consistent with Bassis and Jacobs [2013] who noted that

477 calving is a two step process consisting of (i) ice-shelf rifting that forms an iceberg and
 478 (ii) iceberg detachment. The results here suggest that strong (cross-shore) winds may be
 479 required to drive large tabular icebergs away from their source ice shelves.

480 **4.2 Breaking bonds**

481 The numerical bonds in the LBIM enable the tabular iceberg to retain its shape.
 482 This is demonstrated by comparing the Control simulation to an identical simulation where
 483 all numerical bonds have been removed (Figure 9). In the bond-free simulation, the ice
 484 elements disperse and the calved iceberg quickly loses its original structure. This bond-free
 485 simulation does not adequately represent tabular iceberg, which can move long distances
 486 through the ocean as a cohesive unit. This result motivates the inclusion of bonds in the
 487 LBIM model, even though they are more computationally expensive than traditional point-
 488 iceberg models.

489 By breaking some (but not all) numerical bonds, we can simulate breaking of tab-
 490 ular icebergs into smaller pieces. Figure 10 shows the results of an experiment which is
 491 identical to the Control experiment, except that all numerical bonds that intersect the line
 492 $x = \frac{L_x}{2}$ have also been severed. This effectively cuts the large tabular iceberg into two
 493 halves. As the icebergs drift northwards, the two halves of the tabular iceberg each move
 494 as a cohesive unit, but they are able to move independently of one other (Figure 10). The
 495 two large fragments initially move together, but begin to separate after a few days. The
 496 breaking of a tabular iceberg has the additional effect of increasing the total surface area
 497 of ice exposed to the ocean, thus increasing the total decay rate of the icebergs.

498 **4.3 Ocean response**

499 Since the tabular iceberg is submerged in the ocean, the iceberg calving and drift af-
 500 fects the surrounding ocean. In the Control simulation, as the tabular iceberg drifts north-
 501 ward a warming of the surface waters is observed around the tabular iceberg, with the
 502 largest warming occurring at the ice-shelf front and along the tabular iceberg's rounded
 503 edge (Figure 2). This surface warming is caused by upwelling of the warmer waters from
 504 beneath the ice shelf and iceberg. As the icebergs drifts away from the ice shelf, these
 505 warmer waters remain at the surface, mapping out the iceberg wake (Figure 2). The mo-
 506 tion of the tabular iceberg disturbs the ocean surface, which affects ocean velocities through
 507 out the water column (Figure 11). The elevated shears around the tabular iceberg lead to
 508 increased vertical mixing in the vicinity of the iceberg, which alters the stratification of
 509 the water column (Figure 8), warming the upper ocean. The signature of upwelling wa-
 510 ter in the wake of a drifting tabular iceberg bears some similarity to satellite observations
 511 of streaks of increased ocean color in the wake of tabular iceberg in the Southern Ocean
 512 [Duprat et al, 2016], suggesting that the increased productivity around icebergs may be
 513 driven by upwelling water delivering nutrients to the surface.

514 **4.4 Iceberg melt rates**

515 The increased subsurface velocities and temperatures cause elevated melt rates at
 516 the base of the ice shelf and iceberg (Figure 12). The largest melt rates are observed at
 517 the newly calved ice-shelf front and on the rounded side of the tabular iceberg (Figure
 518 12a), where the iceberg calving has created steep ice cliffs. These sharp ice fronts allow
 519 for large ocean currents (Figure 12c), which drive the elevated melt rates. The elevated
 520 melt rates act to smooth out the ice front over time, making the ice cliff less steep. While
 521 this is likely a real phenomena that could be observed in nature, we should be wary of the
 522 modeled velocities at the ice cliffs, since large changes in ice thicknesses are associated
 523 with numerical pressure gradient errors which can drive spurious motion.

524 The large melt rates along the ice edges are also partly driven by the fact that dif-
 525 ferent melt parametrization are used in the interior and edges of large ice structures (see
 526 Section 2.5). Figure 13 shows the melt rates computed with (a) the 3-equation-model
 527 parametrization [Holland and Jenkins, 1999], (b) point-particle-iceberg-melt parametriza-
 528 tion [Gladstone et al, 2001], and (c) the mixed-melt-rate parametrization (introduced in
 529 Section 2.5). The 3-equation-model melt rates (Figure 13a) are less than a third of the
 530 size of those calculated using the point-particle-iceberg-melt parametrization (Figure 13b).
 531 When the mixed-melt-rate parametrization is used (Figure 13c), the very high melt rates
 532 are only observed at the edges of ice structures.

533 5 Summary

534 In this study we present a novel framework for simulating tabular icebergs in ocean
 535 models, and representing icebergs with finite extent and structure. In this framework, large
 536 tabular icebergs are represented by collections of Lagrangian elements that are held to-
 537 gether by numerical bonds. Each ice element is assigned a surface area and shape, and
 538 can interact with the ocean and other elements in a way which is consistent with the shape
 539 of the element. Such a representation allows tabular icebergs to interact with the ocean
 540 across a wide area (larger than a grid cell), and individual ice elements to behave as if
 541 they had a finite extent. This is in contrast to previous representations of icebergs in nu-
 542 matical models [Jongma et al, 2009; Martin and Adcroft, 2010; Marsh et al, 2015] that
 543 treat icebergs as point particles. Explicitly resolving tabular icebergs in the ocean allows
 544 the icebergs to interact with the ocean in a more realistic way, and allows us to study the
 545 effects that tabular icebergs have on ocean circulation. Including numerical bonds between
 546 elements allows for simulations which emulate iceberg calving and fracture by severing
 547 the bonds.

548 The capabilities of the tabular iceberg model are demonstrated by modeling a tab-
 549 ular iceberg drifting away from an idealized ice shelf (also constructed using Lagrangian
 550 elements). The results show that explicitly resolving tabular icebergs in the ocean allows
 551 for a complex interaction between the iceberg and the surrounding ocean. In our Con-
 552 trol setup, a tabular iceberg is driven away from the ice shelf by ocean currents, wind
 553 stress, and the Coriolis force. As the iceberg moves through the water, it disturbs the
 554 ocean surface, driving ocean currents. The motion of the iceberg and melt beneath the
 555 iceberg drive upwelling along the sides of the iceberg, which entrains ambient water and
 556 causes a warming of the surface ocean in the wake of the iceberg. The changing ocean
 557 conditions feed back onto the iceberg, affecting its motion and melt rates. The highest
 558 melt rates are observed at edge of the iceberg which has the steepest ice cliff. These have
 559 the effect of smoothing out the ice edge over time. Simulations without using numerical
 560 bonds showed that the bonds are essential for allowing the iceberg to move as a unit. We
 561 also demonstrate that by breaking these numerical bonds we can simulate iceberg fracture,
 562 which is important process that increases the rate of iceberg decay.

563 To our knowledge, the model presented in this study is the first model to explicitly
 564 resolve drifting tabular icebergs in an ocean model that can be used for climate studies.
 565 A natural extension of this work is a representation of tabular icebergs in a general cir-
 566 culation model (GCM). However, before this can be done, there are a number of issues
 567 that need to be resolved: firstly, the question of how and when to introduce tabular ice-
 568 bergs into the ocean needs to be addressed. For GCM's with active ice shelves, a calving
 569 law is needed to release the tabular iceberg into the ocean. The question of what calving
 570 law to use is a topic of ongoing research [Benn et all, 2007; Alley et al, 2008; Levermann
 571 et al, 2012; Bassis and Jacobs, 2013] and is still unresolved. One potential way to tem-
 572 porarily bypass this problem would be to run hindcast simulations using historically ob-
 573 served calving events. A related issue is the question of how and when to break the bonds
 574 within the freely floating icebergs to simulate iceberg breakup. Without a rule for iceberg
 575 breakup, the tabular icebergs would likely drift to unrealistically low latitudes. Further

work is also needed to understand (and model) the interactions between tabular icebergs and sea ice, and to parametrize the effects of iceberg grounding, as these interactions play a large role in dictating the trajectories of tabular icebergs. However, despite these remaining challenges, the technical framework described in this article is potentially a useful step towards including tabular icebergs in global GCM's.

6 Appendix A

6.1 Environmental forces on ice elements

The non-interactive forces on an ice element are as described in [Martin and Adcroft, 2010], and are repeated here for completeness. The forces on an element due to air (a), ocean (o) and sea ice (si) drag are given by

$$(\vec{F}_a) = \rho_a (0.5 c_{a,v} W F + c_{a,h} L W) |\vec{u}_a - \vec{u}| (\vec{u}_a - \vec{u}), \quad (11)$$

$$(\vec{F}_o) = \rho_o (0.5 c_{o,v} W (D - T_{si}) F + c_{o,h} L W) |\vec{u}_o - \vec{u}| (\vec{u}_o - \vec{u}), \quad (12)$$

$$(\vec{F}_{si}) = \rho_{si} (0.5 c_{si,v} W T_{si} F + c_{si,h} L W) |\vec{u}_{si} - \vec{u}| (\vec{u}_{si} - \vec{u}). \quad (13)$$

Here ρ_a , ρ_o , ρ_{si} , are the density of air, ocean and sea ice, respectively. $c_{a,v}$, $c_{o,v}$ and $c_{si,v}$ are the vertical drag coefficients with air, ocean and sea ice, while $c_{a,h}$, $c_{o,h}$ and $c_{si,h}$ are the respective horizontal drag coefficients. \vec{u}_a , \vec{u}_o , \vec{u}_{si} , are the velocities air, ocean and sea ice, respectively. L, W, T and D are the length, width, thickness, free-board and draft of the ice element. The element thickness is related to the draft and free-board by $T = F + D$ and $D = \frac{\rho}{\rho_o} T$, where ρ is the ice element density. T_{si} is the sea ice thickness.

The wave radiation force (\vec{F}_R) is given by

$$\vec{F}_R = \frac{1}{2} \rho_o c_{wd} g a \min(a, F) 2 \frac{W L}{W + L} \frac{\vec{v}_a}{|\vec{v}_a|} \quad (14)$$

where g is the acceleration due to gravity, a is the wave amplitude empirically related to the wind speed by $a = 0.010125 |\vec{v}_a - \vec{v}_o|$, and c_{wd} is the wave drag coefficient defined as

$$c_{wd} = 0.06 \min \left(\max \left[0, \frac{L - L_c}{L_t - L_c} \right], 1 \right), \quad (15)$$

where $L_w = 0.32 |\vec{v}_a - \vec{v}_o|^2$ is an empirical wave length, $L_c = 0.125 L_w$ is the cutoff length, and $L_t = 0.25 L_w$ is the upper limit.

The pressure gradient force is approximated as a force due to sea surface slope and given by

$$\vec{F}_{SS} = -M g \vec{\nabla} \eta \quad (16)$$

where η is the sea surface height.

6.2 Melt rate parametrization

As discussed in Section 2.5, unbounded ice elements in the LBIM decay according to parameterizations for iceberg decay typically used in iceberg drift models [Martin and Adcroft, 2010], while ice elements within larger ice structures have only a basal melt given by the three equation model [Holland and Jenkins, 1999].

For unbonded ice elements, the element thickness decays due to basal melt at a rate M_b , while the length and width of the elements decay as a result of melt due to wave erosion, M_e , and melt due to buoyant convection, M_v . Following Gladstone et al [2001] and

Martin and Adcroft [2010], the basal melt rate, wave erosion melt rate, and buoyant convection melt rate are parameterized by

$$M_b = 0.58|\vec{v} - \vec{v}_0|^{0.8} \frac{\tilde{T}_0 - \tilde{T}}{L^{0.2}} \quad (17)$$

$$M_e = \frac{1}{12} S_s \left(1 + \cos [\pi A_i^3] \right) \left(\tilde{T}_0 + 2 \right), \quad (18)$$

$$M_v = \left(7.62 \times 10^{-3} \right) \tilde{T}_0 + \left(1.29 \times 10^{-3} \right) \tilde{T}_0^2. \quad (19)$$

\tilde{T} is the effective iceberg temperature and is set to $\tilde{T} = 4^\circ\text{C}$, \tilde{T}_0 is the temperature at the top of the ocean, A_i is the sea-ice area fraction, and S_s is the sea state, which is given by the Beaufort scale

$$S_s = \frac{2}{3} |\vec{u}_a - \vec{u}_o|^{\frac{1}{2}} + \frac{1}{10} |\vec{u}_a - \vec{u}_o| \quad (20)$$

All three melt rates are in units of meters per day.

For elements inside larger structures, the melt due to wave erosion and melt due to buoyant convection are set to zero, and the basal melt, M_s , is given by the standard three equation model [Holland and Jenkins, 1999].

7 Appendix B

7.1 Modified Verlet Algorithm

The LBIM uses a version velocity Verlet time-stepping algorithm, which has been modified to allow part of the forcing to be calculated implicitly. The traditional velocity Verlet algorithm is commonly used in molecular dynamics, as it is simple to implement, second order accurate and computationally efficient [Swope et al, 1982; Omelyan et al, 2002]. Here we modify the traditional scheme to allow for the drag forces to be modeled implicitly, which prevents large accelerations for element's whose mass approaches zero. To do this, we include both an implicit and explicit acceleration, $a = a^{exp} + a^{imp}$. The explicit acceleration, a^{exp} , includes all forcing terms which depend only on the previous time step and the current position, while the implicit acceleration, a^{imp} , includes forcing terms which depend on the velocity at the current time step (in particular the drag and Coriolis forces).

Using a time step of Δt , and subscripts to denote the time step (so that $t_{n+1} = t_n + \Delta t$), the modified velocity Verlet scheme can be written as:

- 1) Calculate updated position: $x_{n+1} = x_n + u_n \Delta t + \frac{1}{2} \Delta t^2 \left(a_n^{exp} + a_n^{imp} \right)$.
- 2) Calculate a_{n+1}^{exp}
- 3) Calculate a_{n+1}^{imp} and $u_{n+1} = u_n + \frac{\Delta t}{2} \left(a_n^{exp} + a_{n+1}^{exp} \right) + (\Delta t) a_{n+1}^{imp}$

This scheme reduces to the traditional velocity Verlet when a^{imp} is set to zero. Note that $a_{n+1}^{exp} = a_{n+1}^{exp}(x_{n+1}, t_n)$ is an explicit function of x_{n+1} and other quantities evaluated at time t_n , while $a_{n+1}^{imp} = a_{n+1}^{imp}(u_{n+1}, x_{n+1}, t_n)$ additionally depends on u_{n+1} , and needs to be solved implicitly. For this reason in step three, a_{n+1}^{imp} and u_{n+1} need to be solved simultaneously, as described in the next subsection.

In equation (1), the forces due to ocean drag, atmospheric drag and sea ice drag are treated implicitly. The force due to sea surface slope and wave radiation are treated explicitly. The Coriolis term is handled using Crank-Nicolson scheme so that half of the effect is implicit and half is explicit. The elastic part of the interactive forces is treated explicitly, while the interactive damping is handled semi-implicitly in that the drag force on element A by element B depends on the velocities of elements A and B evaluated at time t_{n+1} and t_n , respectively.

652 7.2 Solving for the velocity implicitly

653 Since this modified scheme contains some forcing terms which are handled implicitly,
 654 a_{n+1}^{imp} and u_{n+1} need to be calculated simultaneously. We demonstrate how this is
 655 done, using a simplified one-dimensional version of equation (1), neglecting the atmo-
 656 spheric drag, sea ice drag and Coriolis force, so that the only implicitly treated term is the
 657 ocean drag. In this demonstration, we use a superscript to denote the ocean drag force,
 658 F^o , and ocean velocity, u^o , to avoid confusion with the subscripts indicating time step.
 659 We also define an explicit force, F^{exp} , which accounts for all forces not proportional the
 660 element velocity. With these simplifications, the implicit and explicit accelerations are

$$661 \quad a^{exp} = \frac{1}{M}(\vec{F}^{exp}) \quad (21)$$

$$661 \quad a^{imp} = \frac{1}{M}(F^o) \quad (22)$$

662 The ocean drag force at time t_{n+1} is modeled (mostly) implicitly as

$$663 \quad F_{n+1}^o = \tilde{c}^o |u_n^o - u_n| (u_n^o - u_{n+1}), \quad (23)$$

663 where \tilde{c}^o is the effective drag coefficient, accounting for the dimensions of the ice element
 664 (see equation 12).

665 Step 3 of the modified velocity Verlet scheme can be rewritten by introducing an
 666 intermediate velocity u^* , which only depends on the velocity and acceleration at time t_n ,

$$666 \quad u_n^* = u_n + \frac{1}{2}(\Delta t)a_n^{exp}. \quad (24)$$

667 Using this, the updated velocity (Step 3) can be written

$$668 \quad u_{n+1} = u_n^* + \frac{\Delta t}{2}a_{n+1}^{exp} + (\Delta t)a_{n+1}^{imp}. \quad (25)$$

668 Including the forcing terms into this equations gives

$$669 \quad u_{n+1} = u_n^* + \frac{\Delta t}{2M}(F_{n+1}^{exp}) + \frac{\Delta t}{M} \left(c_w |u_n^o - u_n| (u_n^o - u_{n+1}) \right) \quad (26)$$

670 Solving for $u(t_{n+1})$ in terms of quantities which only depend on the previous time step
 gives

$$671 \quad u_{n+1} = \frac{u_n^* + \frac{\Delta t}{2M}(F_{n+1}^{exp}) + \frac{\Delta t}{M} \left(c_w |u_n^o - u_n| (u_n^o) \right)}{\left(1 + \frac{\Delta t}{M} c_w |u_n^o - u_n| \right)} \quad (27)$$

672 Once the u_{n+1} has been found, it can be used to calculate the explicit and implicit acceler-
 ations, which are required for the next time step.

673 Finally, we note that the the drag term (equation 23) is not entirely implicit, since
 674 the element velocity inside the absolute value is evaluated at time t_n , rather than at time
 675 t_{n+1} . This is done so that we can solve for the updated velocity analytically. One conse-
 676 quence of this is that it can give rise to a small oscillation in the element velocity. This
 677 oscillation is addressed by using a predictive corrective scheme: after solving for a first
 678 guess of the velocity at time t_{n+1} , this estimate of the velocity is used to update the esti-
 679 mate of the drag force (i.e.: inside the absolute value signs). This updated drag, can now
 680 be used to repeat the process described above to find an improved estimate of the velocity.
 681 We found that two iterations were sufficient to remove the unwanted oscillation.

682 The procedure described in this section is easily extended to include more forcing
 683 terms and two dimensions (where it involves inverting a 2×2 matrix).

684 **8 Appendix C**

685 **Connecting bonds across processor boundaries**

686 Since the LBIM is parallelized across multiple processors, it often happens that two
 687 elements on different processes are bonded together. Keeping track of numerical bonds
 688 across processor boundaries requires a lot of book keeping. In this section we describe the
 689 how LBIM handles bonds across processor boundaries.

690 The basics of the bond bookkeeping work as follows: consider an element A and
 691 an element B that are bonded together. Each element has a copy of the bond (a piece of
 692 memory which describes the bond between the two elements), which is stored with the
 693 element. Let A-B be the bond stored by element A, and B-A be the bond stored by ele-
 694 ment B. Bond A-B contains a pointer which points to element B and bond B-A contains a
 695 pointer which points to element A.

696 Consider a situation where element A and B are originally on Processor 1, and then
 697 element B moves to Processor 2. When this occurs, the memory assigned to element B
 698 on processor 1 is removed, and is allocated on Processor 2. This means that the pointer
 699 to element B in bond A-B (stored in element A on Processor 1) is no longer assigned.
 700 Similarly, the pointer to element A in bond B-A (stored in element B on Processor 2) is
 701 no longer assigned. Before the next time step, a halo update occurs, so that the there is
 702 a copy of element A in the halo of Processor 2 and a copy of element B in the halo of
 703 Processor 1. After the halo update, the bonds A-B and B-A have to be reconnected on
 704 both Processor 1 and 2. To aid in reconnecting the bonds, a copy of the grid cell number
 705 of element B is stored in the bond A-B and a copy of the grid cell number of element A
 706 is stored in the bond B-A. We refer to this as the ‘most recent address’. Before a bond
 707 is moved from one processor to another, the ‘most recent address’ is updated, so that the
 708 bond can be reconnected later. To reconnect bond A-B on Processor 1 (for example), we
 709 find the most recent address of element B, and search through the list of elements in the
 710 grid cell corresponding to the most recent address of element B until element B is found.
 711 The pointer to element B in bond A-B is reassigned, and the bond is said to be connected.

712 The reconnected bond A-B (stored in element A) is said to be working properly
 713 when the following four test pass:

- 714 1. The pointer to element B is assigned on bond A-B.
- 715 2. The corresponding bond B-A exists on element B.
- 716 3. A pointer to element A exists in this bond B-A.
- 717 4. The element A which is being pointed to is the same element A where you started.

718 A useful tool for debugging the disconnecting and reconnecting bonds routines is that
 719 each element is assigned a unique number so that elements are easily identified.

720 **Acknowledgments**

721 This study is supported by awards NA08OAR4320752 and NA13OAR439 from the Na-
722 tional Oceanic and Atmospheric Administration, U.S. Department of Commerce. The
723 statements, findings, conclusions, and recommendations are those of the author and do not
724 necessarily reflect the views of the National Oceanic and Atmospheric Administration, or
725 the U.S. Department of Commerce. The simulations in this paper can be reproduced using
726 the MOM6 model code and experimental setups found at https://github.com/sternalon/Iceberg_repository.

727 **References**

- 728 Asay-Davis, X. S., S. L. Cornford, B. K. Galton-Fenzi, R. M. Gladstone, G. H. Gud-
 729 mundsson, D. M. Holland, P. R. Holland, and D. F. Martin (2016), Experimental de-
 730 sign for three interrelated marine ice sheet and ocean model intercomparison projects:
 731 MISMIP v. 3 (MISMIP+), ISOMIP v. 2 (ISOMIP+) and ISOMIP v. 1 (ISOMIP1).
 732 *Geoscientific Model Development* 9, no. 7: 2471.
- 733 Arrigo, K. R., G. L. van Dijken, D. G. Ainley, M. A. Fahnestock, and T. Markus (2002).
 734 Ecological impact of a large Antarctic iceberg. *Geophys. Res. Lett.*, 29(7).
- 735 Alley, R. B., H. J. Horgan, I. Joughin, K. M. Cuffey, T. K. Dupont, B. R. Parizek, S.
 736 Anandakrishnan, and J. Bassis (2008), A simple law for ice-shelf calving. *Science* 322,
 737 no. 5906, 1344-1344.
- 738 Bassis, J. N., and S. Jacobs (2013), Diverse calving patterns linked to glacier geometry.
 739 *Nature Geoscience*, 6(10), 833-836.
- 740 Benn, D. I., C. R. Warren, and R. H. Mottram (2007). Calving processes and the dynam-
 741 ics of calving glaciers. *Earth-Science Reviews*, 82(3), 143-179.
- 742 Bigg, G. R., Wadley, M. R., Stevens, D. P., and Johnson, J. A. (1997), Modeling the dy-
 743 namics and thermodynamics of icebergs. *Cold Regions Science and Technology*, 26(2),
 744 113-135.
- 745 Borstad, C. P., A. Khazendar, E. Larour, M. Morlighem, E. Rignot, M. P. Schodlok, and
 746 H. Seroussi (2012), A damage mechanics assessment of the Larsen B ice shelf prior to
 747 collapse: Toward a physically-based calving law, *Geophys. Res. Lett.*, 39, L18502
- 748 Biddle, L. C., J. Kaiser, K. J. Heywood, A. F. Thompson and A. Jenkins (2015), Ocean
 749 glider observations of iceberg-enhanced biological productivity in the northwestern
 750 Weddell Sea, *Geophys. Res. Lett.*, 42, 459-465.
- 751 De Rydt, J., and G. H. Gudmundsson (2016), Coupled ice shelf ocean modeling and com-
 752 plex grounding line retreat from a seabed ridge. *J. of Geophys. Res.: Earth Surface*,
 753 121(5), 865-880.
- 754 Dunne, J.P., J.G. John,, A.J. Adcroft, S.M. Griffies, R.W. Hallberg, E. Shevliakova, R.J.
 755 Stouffer, W. Cooke, K.A. Dunne, M.J Harrison, and J.P. Krasting (2012), GFDL's
 756 ESM2 global coupled climate-carbon Earth System Models. Part I: Physical formula-
 757 tion and baseline simulation characteristics. *J. of Climate*, 25(19), 6646-6665.
- 758 Depoorter, M. A., J. L. Bamber, J. A. Griggs, J. T. M. Lenaerts, Stefan RM Ligtenberg,
 759 M. R. van den Broek, and G. Moholdt (2013), Calving fluxes and basal melt rates of
 760 Antarctic ice shelves. *Nature*, 502(7469), 89-92.
- 761 Determan J., Gerdes R. (1994), Melting and freezing beneath ice shelves: implications
 762 from a three-dimensional ocean-circulation model. *Ann. Glaciol.*, 20, 413-419.
- 763 Dowdeswell, J. A., and J. L. Bamber (2007), Keel depths of modern Antarctic icebergs
 764 and implications for sea-floor scouring in the geological record. *Marine Geology*,
 765 243(1), 120-131.
- 766 Duprat, L. P., G. R. Bigg, and D. J. Wilton (2016), Enhanced Southern Ocean marine pro-
 767 ductivity due to fertilization by giant icebergs. *Nature Geoscience*.
- 768 Eckert, E. R. G. (1950). Introduction to the Transfer of Heat and Mass. McGraw-Hill.
- 769 Fogwill, C.J., E. van Sebille, E.A. Cougnon, C.S. Turney, S.R. Rintoul, B.K. Galton-Fenzi,
 770 G.F. Clark, E.M. Marzinelli, E.B. Rainsley, and L. Carter (2016), Brief communication:
 771 Impacts of a developing polynya off Commonwealth Bay, East Antarctica, triggered by
 772 grounding of iceberg B09B. *The Cryosphere*, 10(6), p.2603.
- 773 Gladstone, R. M., G. R. Bigg, and K. W. Nicholls. (2001), Iceberg trajectory model-
 774 ing and meltwater injection in the Southern Ocean (1978-2012). *J. of Geophys. Res.:
 775 Oceans*, 106(C9), 19903-19915.
- 776 Goldberg, D. N., C. M. Little, O. V. Sergienko, A. Gnanadesikan, R. Hallberg, and M.
 777 Oppenheimer (2012), Investigation of land ice-ocean interaction with a fully coupled
 778 ice-ocean model: 1. Model description and behavior. *J. of Geophys. Res.: Earth Surface*,
 779 117(F2).

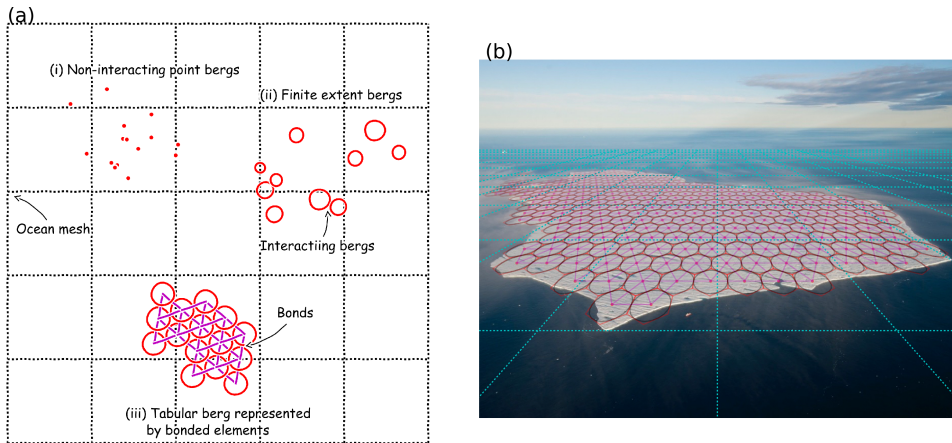
- 780 Gladish, C. V., D. M. Holland, P. R. Holland, and S. F. Price (2012), Ice-shelf basal chan-
781 nels in a coupled ice/ocean model. *J. of Glaciol.*, 58(212), 1227-1244.
- 782 Grosfeld K., R. Gerdes, J. Determan (1997), Thermohaline circulation and interaction
783 between ice shelf cavities and the adjacent open ocean. *J. Phys. Oceanogr.*, **102**, C7,
784 15959-15610.
- 785 Grosfeld, K., and H. SandhŁger, (2004). The evolution of a coupled ice shelfDocean sys-
786 tem under different climate states. *Global and Planetary Change*, 42(1), 107-132.
- 787 Hallberg, R., A. Adcroft, J. P. Dunne, J. P., Krasting, R. J., and Stouffer (2013), Sensitiv-
788 ity of twenty-first-century global-mean steric sea level rise to ocean model formulation.
789 *J. of Climate*, 26(9), 2947-2956.
- 790 Holland D. M., Jenkins A. (2001), Adaptation of an isopycnic coordinate ocean model for
791 the study of circulation beneath ice shelves. *Mon. Wea. Rev.*, 129, 1905-1927.
- 792 Holland P. R. and D. L. Feltham (2006), The effects of rotation and ice shelf topography
793 on frazil-laden Ice Shelf Water plumes. *J. Phys. Oceanogr.*, 36, 2312-2327.
- 794 Holland, D. M., and A. Jenkins (1999), Modeling thermodynamic ice-ocean interactions at
795 the base of an ice shelf. *J. of Phys. Oceanogr.* 29.8, 1787-1800.
- 796 Hellmer H.H., Olbers D. J. (1989), A two-dimensional model for the thermohaline circula-
797 tion under an ice shelf. *Antarctic Science*, 1, 325- 336.
- 798 Henderson J., J. S. P. Loe (2016), The Prospects andChallenges for Arctic Oil Develop-
799 ment. *Oil, Gas and Energy Law Journal (OGEL)*, 14 (2)
- 800 Hopkins, M. A. (1996). On the mesoscale interaction of lead ice and floes. *J. of Geophys.*
801 *Res.: Oceans*, 101(C8), 18315-18326.
- 802 Hopkins, M. A. (2004). A discrete element Lagrangian sea ice model. *Engineering Com-
803 putations*, 21(2/3/4), 409-421.
- 804 Gaskill, H. S., and J. Rochester (1984). A new technique for iceberg drift prediction. *Cold
805 Reg. Sci. Technol.*, 8(3), 223-234.
- 806 Jacobs, S. S., H. H. Helmer, C. S. M. Doake, A. Jenkins, R. M. Frolich (1992), Melting
807 of ice shelves and the mass balance of Antarctica. *J. of Glaciol.*, 38(130), 375-387.
- 808 Jakobsen, T. (2001). Advanced character physics. In *Game Developers Conference*, Vol. 3.
- 809 Jenkins, A., P. Dutrieux, S. S. Jacobs, S. D. McPhail, J. R. Perrett, A. T. Webb, and D.
810 White (2010), Observations beneath Pine Island Glacier in West Antarctica and implica-
811 tions for its retreat. *it Nature Geo.*, 3(7), 468-472.
- 812 Jacobs, S. S., A. Jenkins, C. F. Giulivi, and P. Dutrieux (2011). Stronger ocean circulation
813 and increased melting under Pine Island Glacier ice shelf. *Nature Geo.*, 4(8), 519-523.
- 814 Jongma, J. I., E. Driesschaert, T. Fichefet, H. Goosse, and H. Renssen (2009), The ef-
815 fect of dynamic-thermodynamic icebergs on the Southern Ocean climate in a three-
816 dimensional model, *Ocean Modell.*, 26, 104D113.
- 817 Kubat I., M. Sayed, S. Savage, T. Carrières (2005), An operational model of iceberg drift
818 *Int. J. Off. Polar Eng.*, 15 (2), 125D131
- 819 Lewis E.L. and R.G. Perkin (1986), Ice pumps and their rates. *J. of Geophys. Res.*, 91,
820 11756-11762.
- 821 Losch, M. (2008). Modeling ice shelf cavities in a z coordinate ocean general circulation
822 model. *J. of Geophys. Res.: Oceans*, 113(C8).
- 823 Li, B., H. Li, Y. Liu, A. Wang and S. Ji (2014), A modified discrete element model for
824 sea ice dynamics. *Acta Oceanologica Sinica*, 33(1), 56-63.
- 825 Liu, M. B. and G. R. Liu (2010), Smoothed particle hydrodynamics (SPH): an overview
826 and recent developments. *Archives of computational methods in engineering*, 17(1), 25-
827 76.
- 828 Lichéy, C., and H. H. Hellmer (2001). Modeling giant-iceberg drift under the influence of
829 sea ice in the Weddell Sea, Antarctica. *J. of Glaciol.*, 47(158), 452-460.
- 830 Levermann, A., T. Albrecht, R. Winkelmann, M. A. Martin, M. Haseloff, and I. Joughin.
831 (2012), Kinematic first-order calving law implies potential for abrupt ice-shelf retreat.
832 *The Cryosphere*, 6(2), 273-286.

- 833 Mountain, D. G. (1980). On predicting iceberg drift. *Cold Reg. Sci. Technol.*, 1(3-4), 273-
834 282.
- 835 Martin, T., and Adcroft, A. (2010), Parameterizing the fresh-water flux from land ice to
836 ocean with interactive icebergs in a coupled climate model. *Ocean Modelling*, 34(3),
837 111-124.
- 838 Marsh, R., V. O. Ivchenko, N. Skliris, S. Alderson, G. R. Bigg, G. Madec, A. T. Blaker
839 Y. Aksenov, B. Sinha, A.C. Coward, and J.L. Sommer (2015), NEMODICB (v1. 0):
840 interactive icebergs in the NEMO ocean model globally configured at eddy-permitting
841 resolution. *Geoscientific Model Development* 8, no. 5 (2015): 1547-1562.
- 842 MacAyeal D.R. (1984), Thermohaline Circulation Below the Ross Ice Shelf: A Conse-
843 quence of Tidally Induced Vertical Mixing and Basal Melting. *J. Geophys. Res.*, 89,
844 597-606
- 845 Merino, N., Le Sommer, J., Durand, G., Jourdain, N. C., Madec, G., Mathiot, P., and
846 Tournadre, J. (2016), Antarctic icebergs melt over the Southern Ocean: climatology and
847 impact on sea ice. *Ocean Modelling*, 104, 99-110.
- 848 Nicholls K.W. (1996), Temperature variability beneath Ronne Ice Shelf, Antarctica, from
849 thermistor cables. *J. Phys. Oceanogr.*, 11, 1199-1210.
- 850 Nicholls KW, Østerhus S, Makinson K (2009), Ice-Ocean processes over the continental
851 shelf of the southern Weddell Sea, Antarctica: a review. *Rev. Geophys.* 47(3).
- 852 Omelyan, I. P., M. I. Mryglod, and R. Folk (2002), Optimized Verlet-like algorithms for
853 molecular dynamics simulations. *Physical Review E*, 65(5), 056706.
- 854 Pizzolato, L., S. E. Howell, C. Derksen, J. Dawson, L. Copland (2014), Changing sea ice
855 conditions and marine transportation activity in Canadian Arctic waters between 1990
856 and 2012, *Climatic Change* 123 (2), 161173.
- 857 Pan, W., A. M. Tartakovsky, and J. J. Monaghan (2013). Smoothed particle hydrodyna-
858 mics non-Newtonian model for ice-sheet and ice-shelf dynamics. *J. of Comp. Phys.*, 242,
859 828-842.
- 860 Pralong, A., and M. Funk (2005), Dynamic damage model of crevasse opening and appli-
861 cation to glacier calving, *J. Geophys. Res.*, 110, B01309.
- 862 Rabatel, M., S. LabbÓ and J. Weiss (2015), Dynamics of an assembly of rigid ice floes. *J.*
863 *of Geophys. Res.: Oceans*, 120(9), 5887-5909.
- 864 Rackow, T., C. Wesche, R. Timmermann, H. H. Hellmer, S. Juricke and T. Jung (2017), A
865 simulation of small to giant Antarctic iceberg evolution: differential impact on climatol-
866 ogy estimates. *J. of Geophys. Res.: Oceans*, doi: 10.1002/2016JC012513
- 867 Rignot, E., S. Jacobs, J. Mouginot, and B. Scheuchl (2013), Ice-shelf melting around
868 Antarctica. *Science*, 341, no. 6143 (2013): 266-270.
- 869 Robinson, N. J., M. J. M. Williams, P. J. Barrett, and A. R. Pyne (2010), Observations of
870 flow and ice-ocean interaction beneath the McMurdo Ice Shelf, Antarctica, *J. Geophys.*
871 *Res.*, 115, C03025
- 872 Sergienko, O. V. (2013). Basal channels on ice shelves. *J. of Geophys. Res.: Earth Surface*,
873 118(3), 1342-1355.
- 874 Silva, T. A. M., Bigg, G. R., and Nicholls, K. W. (2006), Contribution of giant icebergs to
875 the Southern Ocean freshwater flux. *J. of Geophys. Res.: Oceans*, 111(C3).
- 876 Smith, K., B. Robison, J. Helly, R. Kaufmann, H. Ruhl, H., T. Shaw, and M. Vernet
877 (2007), Free-drifting icebergs: Hotspots of chemical and biological enrichment in the
878 Weddell Sea, *Science*, 317, 478-482.
- 879 Shepherd, A., and D. Wingham (2007). Recent sea-level contributions of the Antarctic and
880 Greenland ice sheets. *Science*, 315(5818), 1529-1532.
- 881 Stern, A., D. M. Holland, P. R. Holland, A. Jenkins and J. Sommeria (2014), The effect of
882 geometry on ice shelf ocean cavity ventilation: a laboratory experiment. *Experiments in*
883 *Fluids*, 55(5), 1-19.
- 884 Stern, A., Johnson, E., Holland, D.M., Wagner, T.J., Wadhams, P., Bates, R., Abrahamsen,
885 E.P., Nicholls, K.W., Crawford, A., Gagnon, J. and Tremblay, J.E. (2015), Wind-driven
886 upwelling around grounded tabular icebergs. *J. of Geophys. Res.: Oceans*, 120(8), 5820-

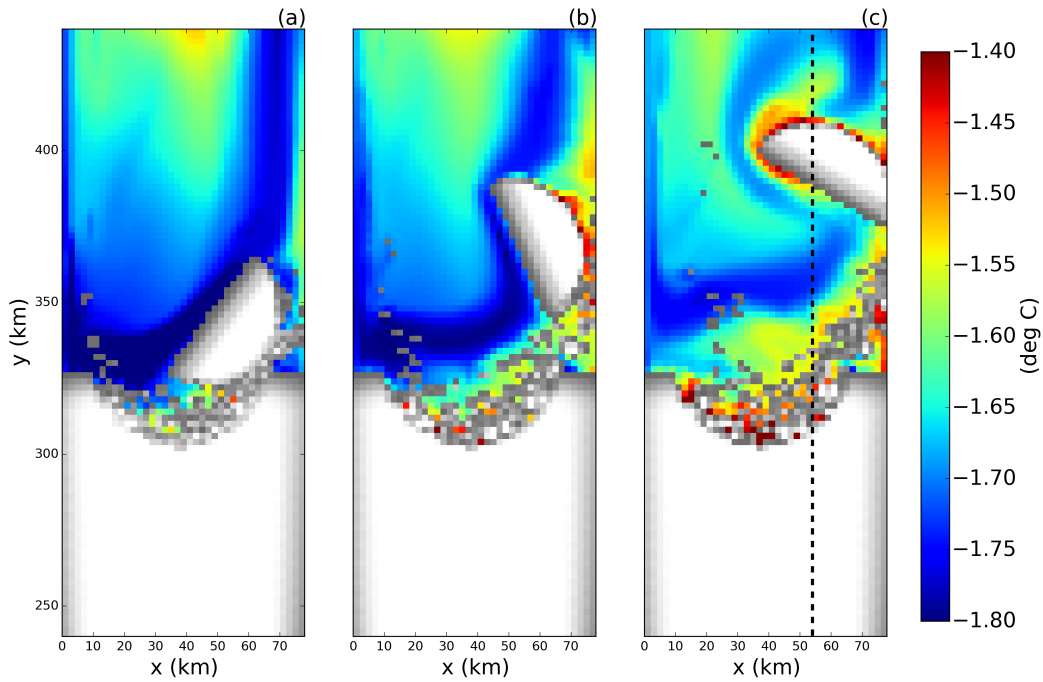
- 887 5835.
- 888 Stern, A., A. Adcroft, and O. Sergienko (2016), The effects of Antarctic iceberg calving
889 size distribution in a global climate model. *J. of Geophys. Res.: Oceans*, 121(8), 5773-
890 5788.
- 891 Swope, W. C., H. C. Andersen, P. H. Berens, and K. R. Wilson (1982), A computer sim-
892 ulation method for the calculation of equilibrium constants for the formation of physi-
893 cal clusters of molecules: Application to small water clusters. *The Journal of Chemical*
894 *Physics* 76, no. 1, 637-649.
- 895 Tournadre, J., N. Bouhier, F. Girard-Ardhuin, and F. RÓmy (2016), Antarctic icebergs dis-
896 tributions 1992-2014. *J. Geophys Res: Oceans*.
- 897 Turnbull I.D., N. Fournier, M. Stolwijk, T. Fosnaes, D. McGonigal (2015), Operational
898 iceberg drift forecasting in Northwest Greenland, *Cold Reg. Sci. Technol.* 110, 1-18
- 899 Unger, J. D., 2014. Regulating the Arctic Gold Rush: Recommended Regulatory Reforms
900 to Protect Alaska's Arctic Environment from Offshore Oil Drilling Pollution . *Alaska L.*
901 *Rev*, 31
- 902 Vernet, M., et al. (2012), Islands of ice: Influence of free-drifting Antarctic icebergs on
903 pelagic marine ecosystems, *Oceanography*, 25(3), 38-39
- 904 Wagner, T. J., Wadhams, P., Bates, R., Elosegui, P., Stern, A., Vella, D., E. P. Abraham-
905 sen, A. Crawford, and Nicholls, K. W. (2014), The ÓfootlooseÓ mechanism: Iceberg
906 decay from hydrostatic stresses. *Geophys. Res. Lett.*, 41(15), 5522-5529.
- 907 Weeks, W. F., and W. J. Campbell (1973). Icebergs as a fresh-water source: an appraisal.
908 *J. of Glaciol.*, 12(65), 207-233.
- 909 White, L., A. Adcroft, and R. Hallberg (2009), High-order regridding-remapping schemes
910 for continuous isopycnal and generalized coordinates in ocean models. *J. of Comp.*
911 *Phys.*, 228(23), 8665-8692.

Parameter	Symbol	Value	Unit
Domain Length	L_x	80	km
Domain Width	L_y	480	km
Horizontal Resolution	Δx	2	km
Number of vertical layers	N_l	72	non-dim
Horizontal Viscosity	ν_H	6.0	$m^2 s^{-1}$
Diapycnal Viscosity	ν_V	10^{-3}	$m^2 s^{-1}$
Horizontal Diffusivity	ϵ_H	1.0	$m^2 s^{-1}$
Diapycnal Diffusivity	ϵ_V	5×10^{-5}	$m^2 s^{-1}$
Initial Surface Temperature	T_t	-1.9	$^{\circ}C$
Initial Bottom Temperature	T_b	1.0	$^{\circ}C$
Initial Surface Salinity	S_t	33.8	psu
Initial Bottom Salinity	S_b	34.7	psu
Maximum Ocean depth	H_{ocean}	720	m
Relaxation Time of Sponge Layer	T_{sponge}	0.1	days
Length of Sponge Layer	L_{sponge}	10	km
LBIM Time Step	dt	10	s
Elastic interactive force spring constant	κ_e	10^{-5}	$kg s^{-2}$

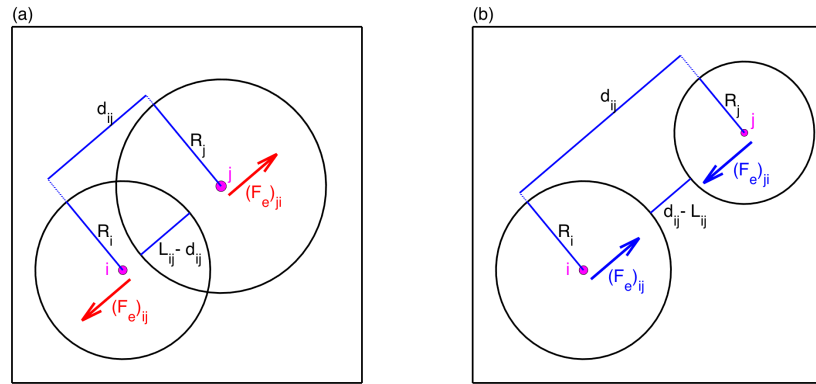
912 **Table 1.** Parameters used in the model. The ocean model parameters are as described in Asay-Davis et al
 913 [2016]



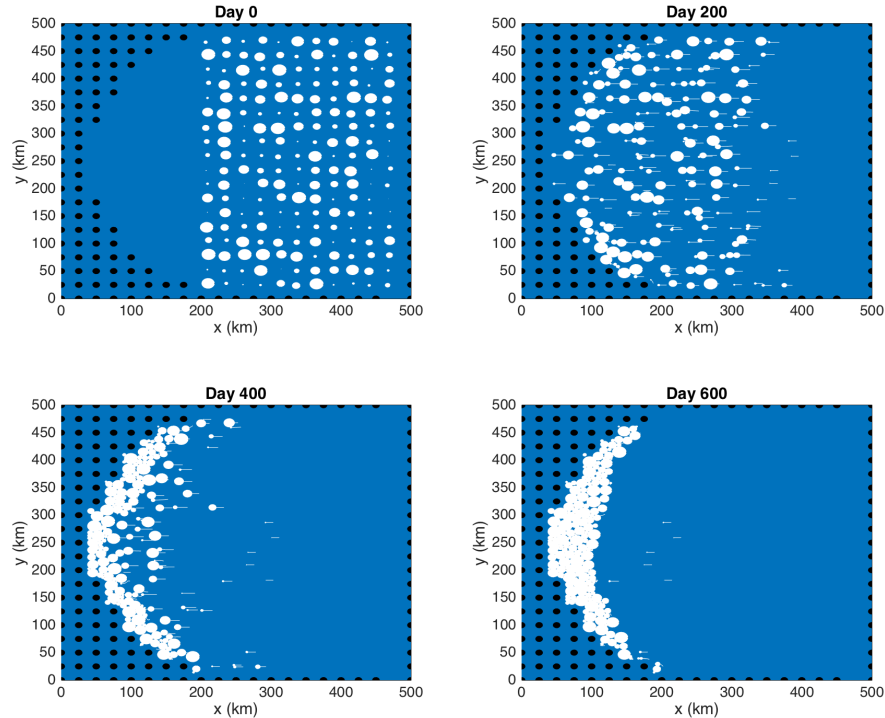
914 **Figure 1.** Schematic showing how tabular icebergs are constructed using Lagrangian elements. (a) Hierar-
 915 chy of ice elements' physical structure: (i) Previous icebergs models represent icebergs using non-interacting
 916 point-particle elements; (ii) In the LBIM ice elements are given finite extent so that they are able to inter-
 917 act with the ocean across multiple grid cells, and can interact with other elements; (iii) These finite extent
 918 elements can be join together by numerical bonds (magenta lines) to form larger structures such as tabular
 919 icebergs. (b) Areal photograph of a tabular iceberg with elements superimposed over it to illustrate how
 920 the Lagrangian elements can be used to model tabular icebergs. In this schematic the ice elements (purple
 921 dots) are initialized in a staggered lattice covering the surface area of the iceberg. For purposes of mass ag-
 922 gregation, the ice elements are assumed to have hexagonal shape (red hexagons). For purposes of element
 923 interactions, the ice elements are assumed to be circular (black circles). Elements are initially bonded to adja-
 924 cent elements using numerical bonds (magenta lines). These numerical bonds form equilateral triangles which
 925 give the shape rigidity. An ocean grid has been included (dashed cyan lines).The background photo is an areal
 926 photograph of iceberg PIIB (Area= 42 km²) taken in Baffin Bay in 2012. A red ship can be identified on the
 927 bottom of the photo for scale.



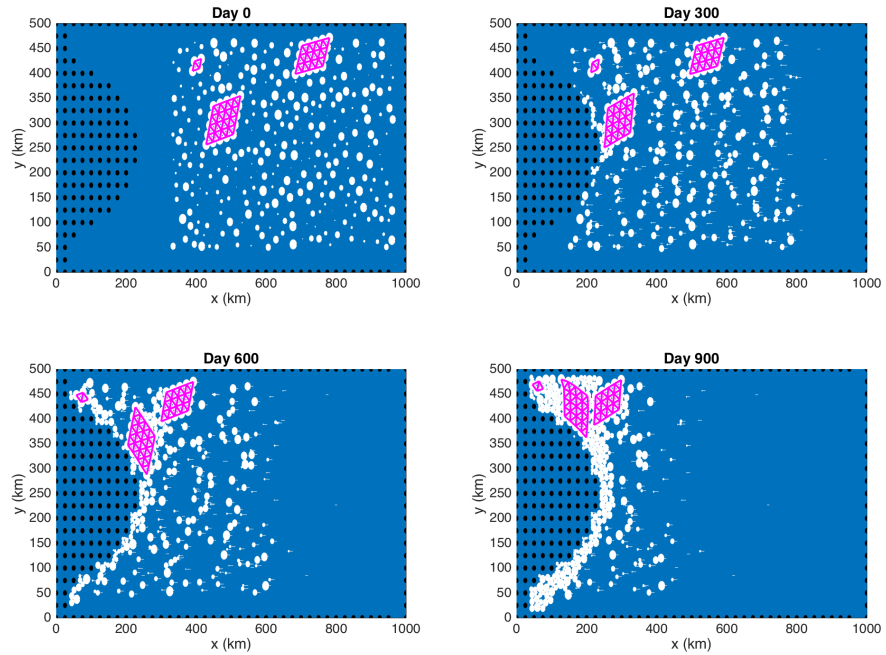
928 **Figure 2.** Snapshots of the sea surface temperature in the LBIM tabular iceberg calving simulation. Snap-
929 shots are taken (a) 7, (b) 15, and (c) 30 days after calving. Grid cells with ice mass $> 10^4$ kg are plotted in
930 white, with grey shading indicating thinner ice. The dashed line in panel (c) shows the location of the vertical
931 transects shown in Figures 8 and 11.



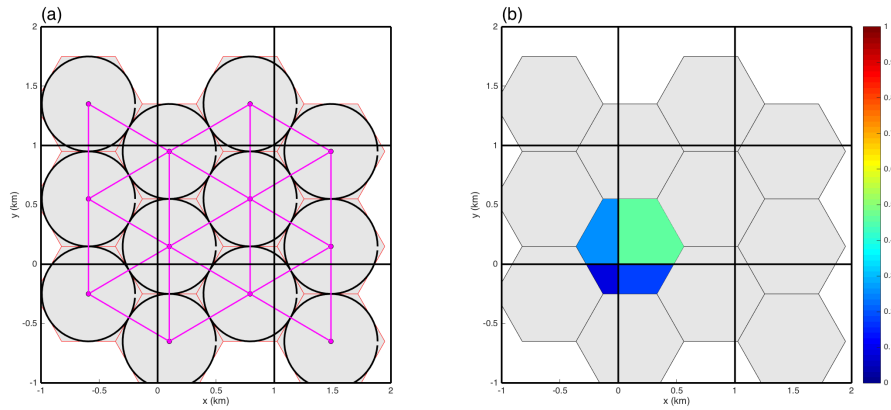
932 **Figure 3.** Diagram showing the (a) repulsive and (b) attractive elastic interactive forces between two ele-
 933 ments, i and j . R_i and R_j are the interactive radii of element i and j , respectively. d_{ij} is the distance between
 934 the centers of elements. $L_{i,j} = R_i + R_j$ is the critical-interaction-length scale. $(F_e)_{ij}$ and $(F_e)_{ji}$ are the elastic
 935 forces applied to elements i and j , respectively (equation 7). A frictional damping force is also applied, which
 936 opposes the relative velocity of the elements (not shown). The attractive forces are only applied when the two
 937 elements are bonded together (i.e.: $B_{ij} = 1$).



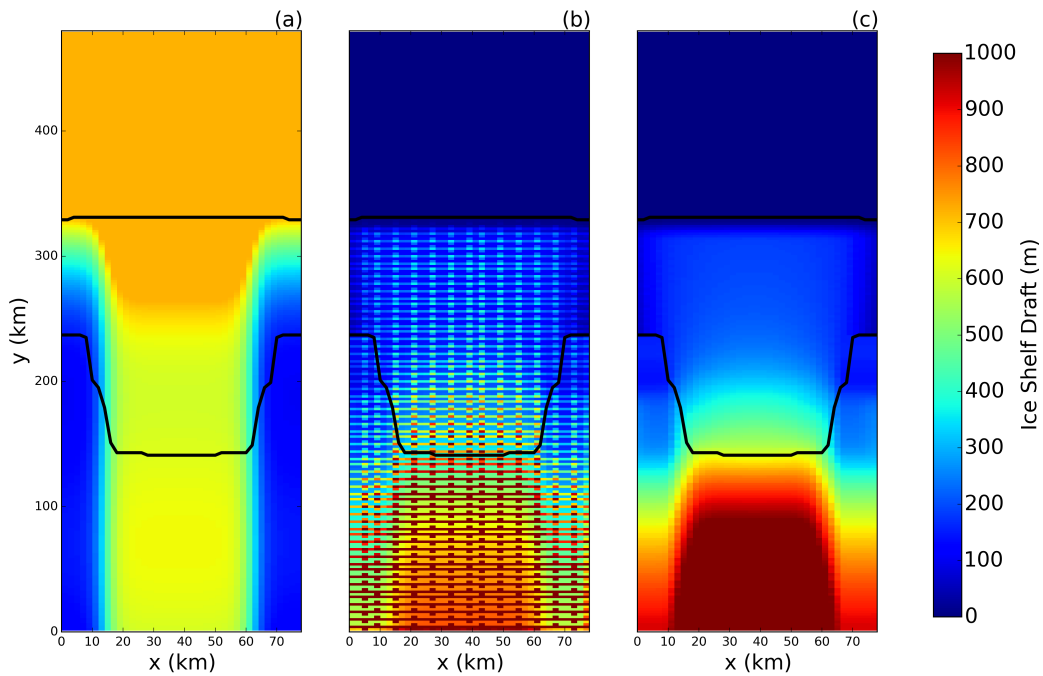
938 **Figure 4.** Results of an ice-only LBIM simulation with no bonds between ice elements. Ice elements are
 939 initialized throughout the domain, as shown in top left panel. The elements are forced by an imposed west-
 940 ward ocean current of $u=0.1\text{m/s}$ (no ocean model is used). Forces due to sea surface slope, atmospheric drag,
 941 Coriolis and sea ice drag are set to zero. The figure shows snapshots of ice element positions at time $t=0, 200,$
 942 400 and 600 days. The size of the dots shows the surface area (and interaction radius) of each ice element.
 943 The white tails behind the elements show the elements' positions over the preceding two days. Land points
 944 are shown by black circles.



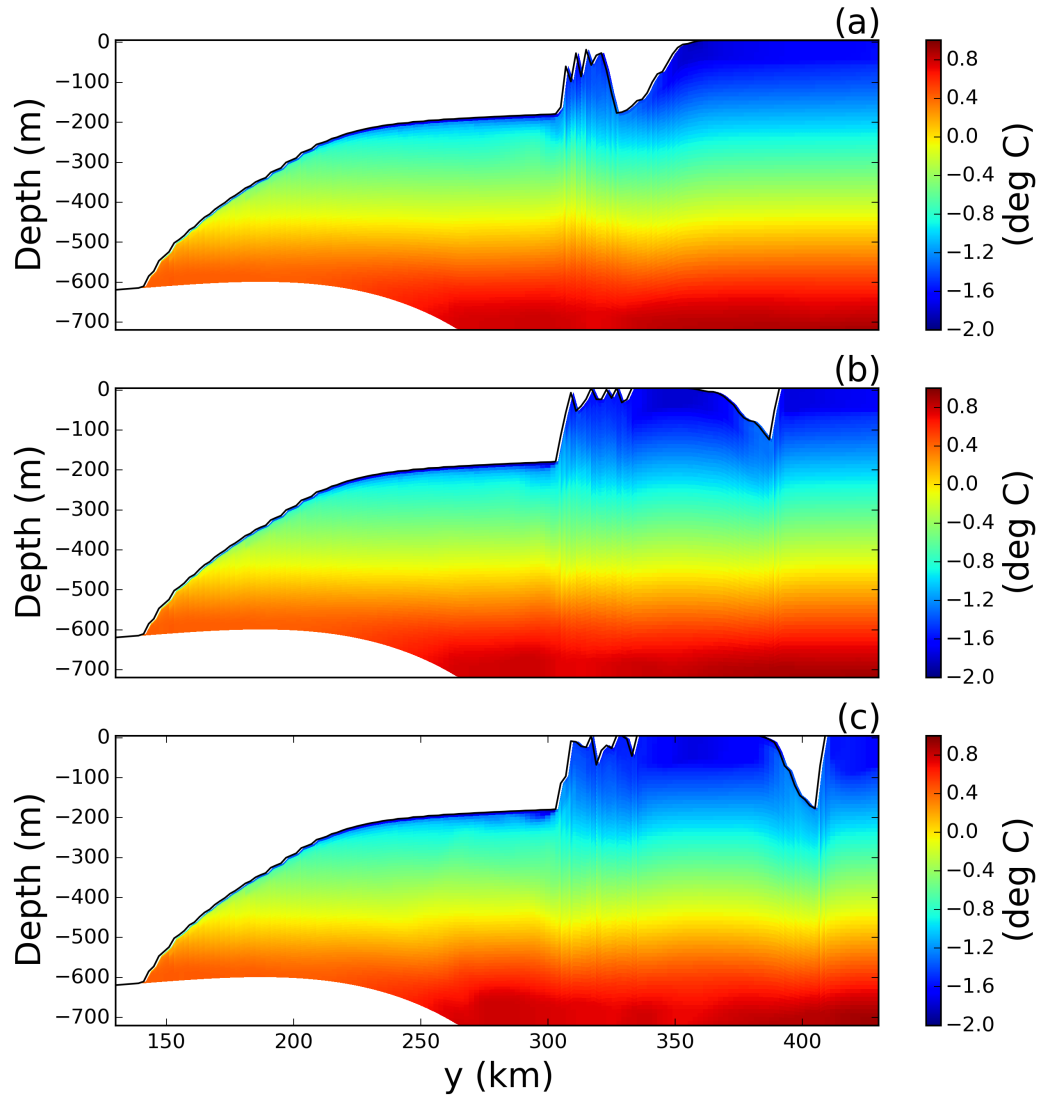
945 **Figure 5.** Results of an ice-only LBIM simulation using bonds between elements. Ice elements are initial-
 946 ized throughout the domain, as shown in top left panel. Three tabular icebergs are included, with 25, 16 and 4
 947 elements respectively. The elements are forced by an imposed westward ocean current of $u=0.1\text{m/s}$ (no ocean
 948 model is used). Forces due to sea surface slope, atmospheric drag, Coriolis and sea ice drag are set to zero.
 949 The figure shows snapshots of ice element positions at time $t=0, 300, 600$, and 900 days. The size of the dots
 950 shows the surface area (and interaction radius) of each ice element. The white tails behind the elements show
 951 the elements' positions over the preceding two days. Bonds between ice elements are plotted in magenta.
 952 Land points are shown by black circles.



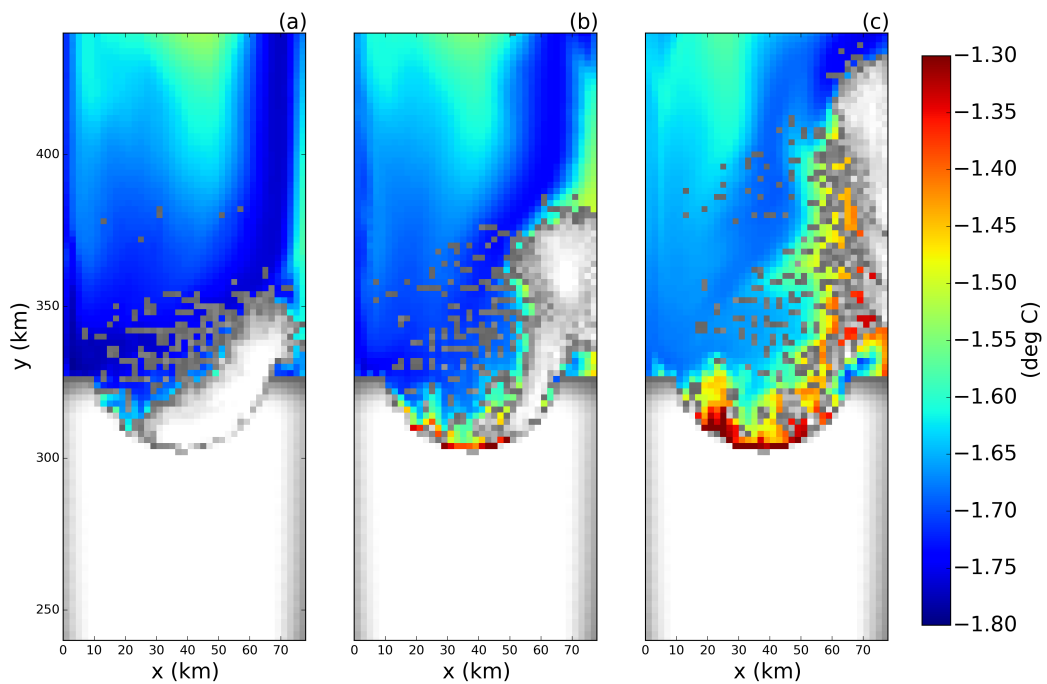
953 **Figure 6.** (a) Ice element packing and geometry: ice elements (purple dots) are initialized in a stag-
954 gered lattice. For purposes of mass aggregation, the ice elements are assumed to have hexagonal shape (red)
955 hexagons). For purposes of element interactions, the ice elements are assumed to be circular (black circles). Elements
956 are initially bonded to adjacent elements using numerical bonds (magenta lines). (b) Intersection
957 of an hexagonal element and the ocean grid. The colors indicate the fraction of the hexagon that lies in each
958 grid cell. These fractions are used as weights to spread LBIM properties to the ocean grid (see text for more
959 details).



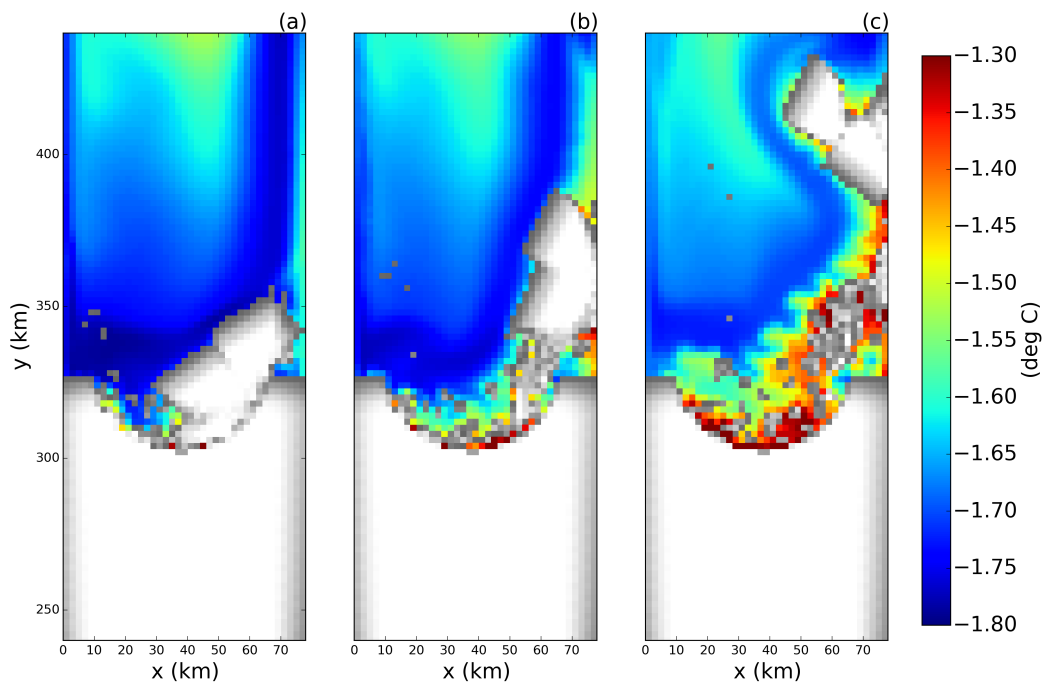
960 **Figure 7.** (a) Ocean bottom topography and (c) ice-shelf draft used to initialized the tabular iceberg calv-
 961 ing simulation. The ice draft is calculated from the total mass in an ocean grid cell after the mass-spreading
 962 interpolation has been applied (as explained in Section 2.3). Panel (b) shows the initial ice draft that would be
 963 calculated if the mass-spreading interpolation were not used (i.e. elements treated as point masses).



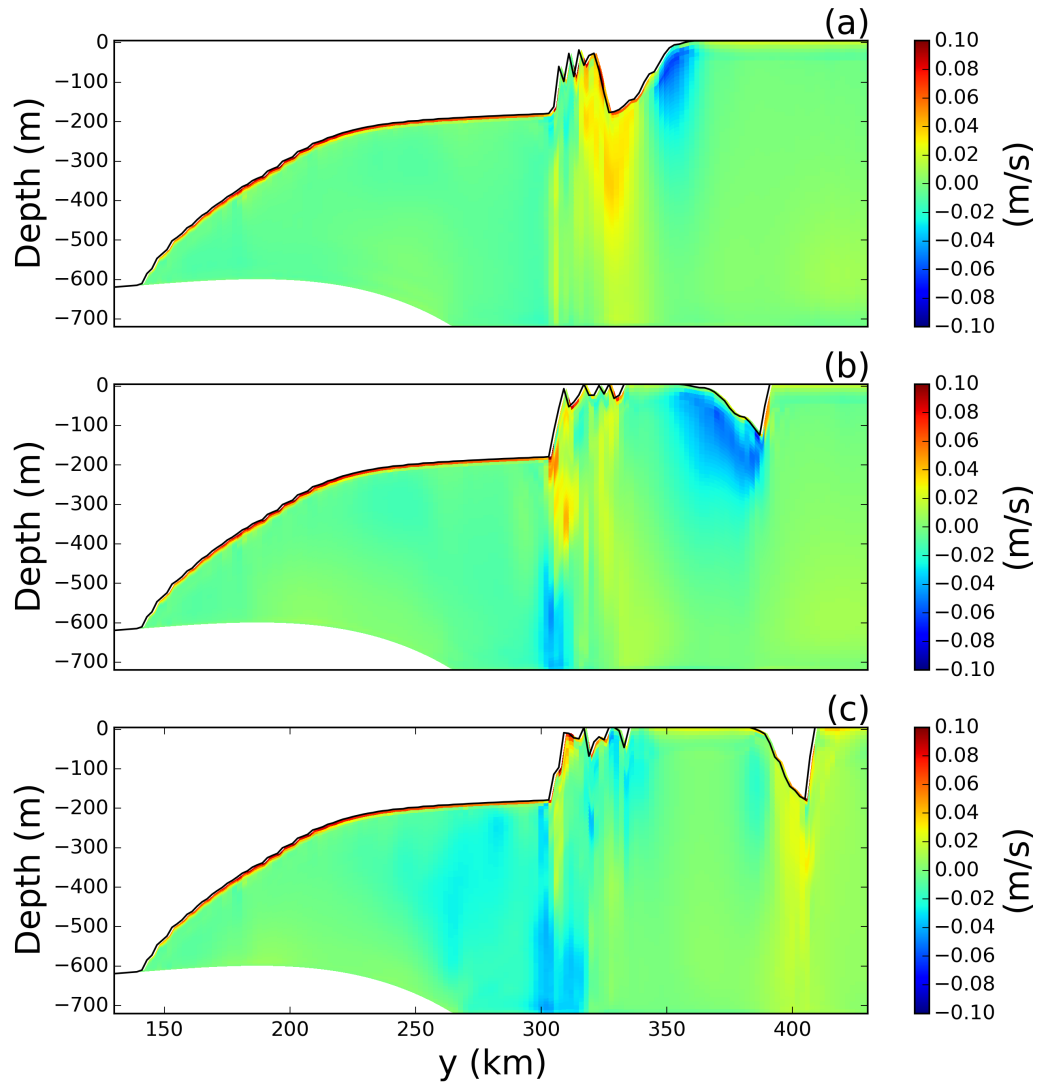
964 **Figure 8.** Snapshots of vertical sections of ocean temperature at $x=54$ km in the tabular-iceberg-calving
965 Control experiment. Snapshots are taken (a) 7, (b) 15, and (c) 30 days after calving. The position of the
966 vertical transects is shown by the dashed lines in Figure 2c.



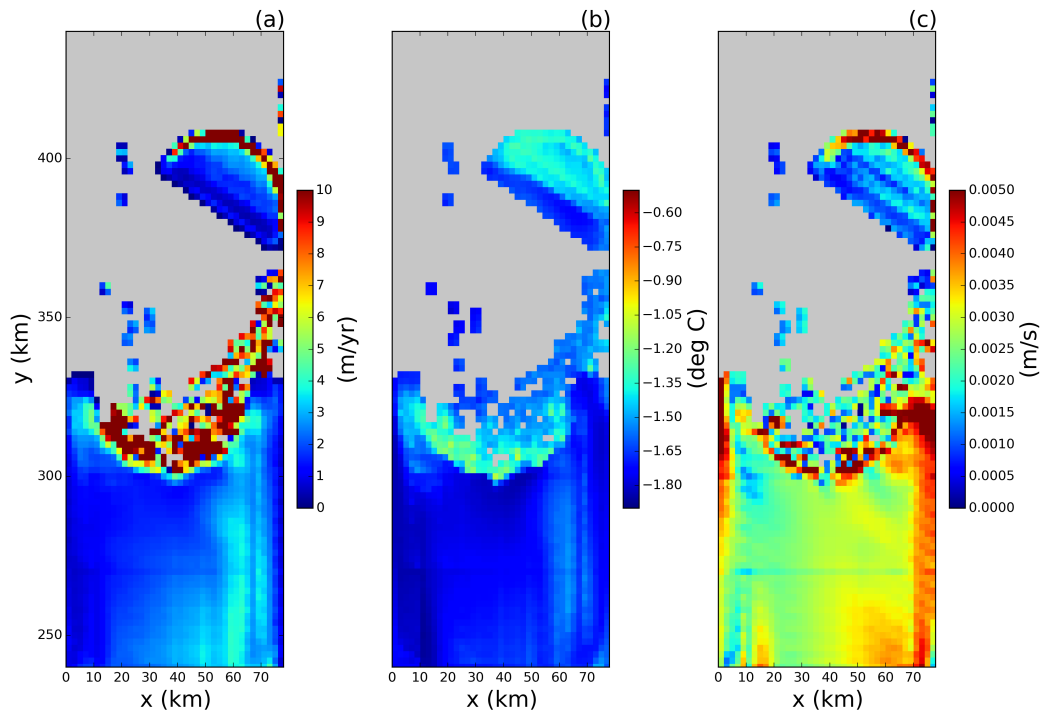
967 **Figure 9.** No bonds simulation: Snapshots of the sea surface temperature for a simulation where all bonds
968 have been broken. Snapshots are taken (a) 7, (b) 15, and (c) 30 days after calving. Grid cells with ice mass >
969 10^4 kg are plotted in white, with grey shading indicating thinner ice.



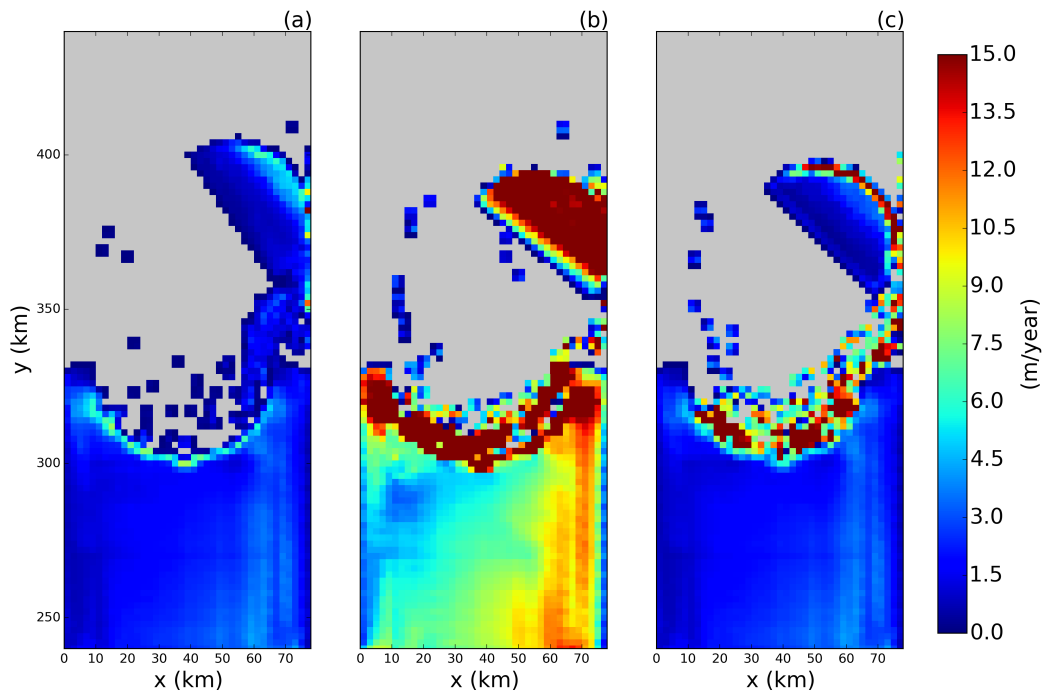
970 **Figure 10.** Iceberg splitting simulation: Snapshots of the sea surface temperature for the iceberg splitting
971 simulation. Snapshots are taken (a) 7, (b) 15, and (c) 30 days after calving. Grid cells with ice mass $> 10^4$ kg
972 are plotted in white, with grey shading indicating thinner ice.



973 **Figure 11.** Snapshots of vertical sections of meridional velocity at $x=54$ km in the tabular-iceberg-calving
 974 Control experiment. Snapshots are taken (a) 7, (b) 15, and (c) 30 days after calving. The position of the
 975 transects is shown by the dashed line in Figure 2c.



976 **Figure 12.** Results of the tabular-iceberg-calving experiment 30 days after the iceberg calves. The three
977 panels show snapshots of the (a) melt rate, (b) top-of-ocean temperature and (c) u^* at the base of the ice shelf.
978 Ocean grid cells without ice are masked out in grey.



979 **Figure 13.** Results of the tabular-iceberg-calving experiment using three different melt-rate parametra-
980 tion. Panels show snapshots of the melt rate 30 days after calving for simulations using the (a) three-equation
981 melt-rate parametrization, (b) icebergs-drift melt-rate parametrization, (c) mixed-melt-rate parametrization (as
982 described in Section 2.5.). Ocean grid cells without ice are masked out in grey.

983 **9 Supplementary Material**

984 The experiment configuration used to initialize the calving-tabular-iceberg simulation
985 (in this study) is the same as that of the Ocean0 setup in the MISOMIP, with the follow-
986 ing three changes made:

- 987 1. The ‘calving criteria’ used in the MISOMIP study (which states that all points in
988 the ice shelf with thickness less than 100m are set to zero thickness) has not been
989 used.
- 990 2. The ice shelf has been thickened on the flanks of the domain, so that the latitude of
991 the grounding line increases away from the center of the ice shelf.
- 992 3. The ice shelf is configured to be symmetric about its meridional center line ($x =$
993 $\frac{L_x}{2}$). This was achieved by using the average of the left and right flanks of the ice-
994 shelf thickness.

995 These three changes were made in order to make the circulation beneath the ice shelf eas-
996 ier to interpret.